ARTICLE

Persister state-directed transitioning and vulnerability in melanoma

Heike Chauvistré [1,2], Batool Shannan[1,2], Sheena M. Daignault-Mill[3], Robert J. Ju[3], Daniel Picard[2,4,5,6], Stefanie Egetemaier [1,2], Renáta Váraljai [1,2], Christine S. Gibhardt [7], Antonio Sechi [8], Farnusch Kaschani [9,10], Oliver Keminer [11,12], Samantha J. Stehbens [3], Qin Liu [13], Xiangfan Yin[13], Kirujan Jeyakumar [14], Felix C. E. Vogel [1,2,20], Clemens Krepler[13], Vito W. Rebecca [13], Linda Kubat [2,15], Smiths S. Lueong[2,16], Jan Forster[2,17], Susanne Horn[1,2], Marc Remke[2,4,5,6], Michael Ehrmann [10,18], Annette Paschen [1,2], Jürgen C. Becker [1,2,15], Iris Helfrich[1,2], Daniel Rauh [14], Markus Kaiser [9,10], Sheraz Gul [11,12], Meenhard Herlyn [13], Ivan Bogeski[7], José Neptuno Rodríguez-López [19], Nikolas K. Haass [3], Dirk Schadendorf [1,2,10] & Alexander Roesch [1,2,10✉]

Melanoma is a highly plastic tumor characterized by dynamic interconversion of different cell identities depending on the biological context. Melanoma cells with high expression of the H3K4 demethylase KDM5B (JARID1B) rest in a slow-cycling, yet reversible persister state. Over time, KDM5B^{high} cells can promote rapid tumor repopulation with equilibrated KDM5B expression heterogeneity. The cellular identity of KDM5B^{high} persister cells has not been studied so far, missing an important cell state-directed treatment opportunity in melanoma. Here, we have established a doxycycline-titratable system for genetic induction of permanent intratumor expression of KDM5B and screened for chemical agents that phenocopy this effect. Transcriptional profiling and cell functional assays confirmed that the dihydropyridine 2-phenoxyethyl   4-(2-fluorophenyl)-2,7,7-trimethyl-5-oxo-1,4,5,6,7,8-hexa-hydro-quinoline-3-carboxylate (termed Cpd1) supports high KDM5B expression and directs melanoma cells towards differentiation along the melanocytic lineage and to cell cycle-arrest. The high KDM5B state additionally prevents cell proliferation through negative regulation of cytokinetic abscission. Moreover, treatment with Cpd1 promoted the expression of the melanocyte-specific tyrosinase gene specifically sensitizing melanoma cells for the tyrosinase-processed antifolate prodrug 3-O-(3,4,5-trimethoxybenzoyl)-(–)-epicatechin (TMECG). In summary, our study provides proof-of-concept for a dual hit strategy in melanoma, in which persister state-directed transitioning limits tumor plasticity and primes melanoma cells towards lineage-specific elimination.

---

*A list of author affiliations appears at the end of the paper.

Cellular plasticity describes the capacity of cells to switch from one phenotype to another and is considered a major driver of non-genetic tumor evolution. Recent time-resolved transcriptomic profiling points to an understanding particularly of melanoma as a heterogeneous ecosystem that dynamically transitions through variably differentiated persister states to escape from exogenous pressure such as debulking therapies[1–3].

One hallmark of persister cells across different cancers is that they transiently rest in a chromatin-mediated slow-cycling state characterized by a high, but reversible nuclear expression of histone H3 lysine demethylases (KDMs)[4–6]. Other features of persister cells are maintenance of embryonic survival or metabolic programs balancing their dependency on oxidative mitochondrial respiration and detoxification of oxygen and lipid radicals[5,7,8]. To date, the majority of studies have focused on the selective elimination of persister cells as small subsets within the total tumor population by exploiting single vulnerabilities like fatty acid oxidation, autophagy, or ferroptosis[9–11]. Previous approaches to selectively eliminate H3K4 demethylase-expressing melanoma cells (KDM5B^{high}), e.g., based on their biological dependence on oxidative ATP production, showed some effect, but suffered from the high metabolic flexibility of this tumor entity[12,13]. Surprisingly, the cellular identity of KDM5B^{high} melanoma persisters has not been unraveled so far, missing an important treatment opportunity. Moreover, strategies to manipulate the dynamics in phenotype switching of persister cells and to combine those with cell identity-specific elimination are lacking in the field.

Melanomas are usually characterized by a continuous expression spectrum of KDM5B^{high}, KDM5B[intermediate] and KDM5B^{low} cells. In comparison, benign melanocytic nevi express KDM5B at high levels across the majority of cells[14]. Single-sorted melanoma cells can rapidly re-establish KDM5B heterogeneity irrespective of their initial KDM5B expression level[15]. Even the pronounced enrichment for KDM5B^{high} states, which is typically seen under cytotoxic stress in vitro and in vivo[5,16,17], rapidly reverts to normal distribution in surviving melanoma cells. This suggests that slow-cycling KDM5B^{high} persister cells represent a transient source for tumor repopulation, but longevity of melanoma requires a dynamic KDM5B tumor composition.

Altogether, this indicates that the slow-cycling KDM5B^{high} persister state could have different, maybe even opposing effects on tumor fate depending on the biological context and might be exploited as a therapeutic target for tumor elimination strategies in melanoma. In this study, we have systematically investigated (i) the actual differentiation phenotype of the KDM5B^{high} melanoma persister state, (ii) the consequences of forcing melanoma cells to ectopically express KDM5B at high levels without the chance to spontaneously revert to normal expression heterogeneity and (iii) whether KDM5B-directed cell state transitioning can be used as a therapeutic vulnerability.

Results

Models for enforced and persistent intratumor expression of KDM5B^{high} states.
KDM5B expression in melanoma is usually heterogeneously distributed, whereas benign melanocytic nevi express KDM5B at high levels across the majority of cells (Fig. 1a[15]). High KDM5B expression in melanoma is significantly associated with poor patient survival (Fig. 1b), while other KDM5 family members lack such an association (Supplementary Fig. 1a). In other cancer entities, KDM5B is inconsistently associated with survival (Supplementary Fig. 1b). To create an experimental model that allows the exogenous induction of KDM5B protein expression, we cloned a Tet-On 3G-system, in which

KDM5B expression is driven by a doxycycline-inducible P_{TRE3G} promoter and established stable melanoma cell clones (WM3734[Tet3G-KDM5B] and WM3734[Tet3G-EGFP] control, Supplementary Fig. 2a–c). After clonal expansion and doxycycline induction, we observed a dose-dependent upregulation of KDM5B mRNA and protein level (Fig. 1c and Supplementary Fig. 2c), concomitant with an inverse decrease in H3K4me3 protein levels confirming the expression of functional KDM5B (Supplementary Fig. 2d). The KDM5B protein level was stably upregulated under continuous doxycycline treatment for at least 3 weeks (Supplementary Fig. 2d). KDM5B immunostaining showed a shift towards increased signals across the majority of WM3734[Tet3G-KDM5B] cells (Fig. 1d). From here on, we denote this scenario as enforced KDM5B^{high} cell state.

To obtain a second, independent method for the modulation of KDM5B expression, which additionally allows simple application to several melanoma cell lines or in vivo, we developed a cell-based compound screening assay applying our previously published *KDM5B-promoter-EGFP*-reporter construct stably expressed in WM3734 melanoma cells (WM3734[KDM5Bprom-EGFP] cells[15], Supplementary Fig. 3a). This fluorescence-based model facilitated monitoring the dynamic nature of the KDM5B transcription state. After screening a 7500-compound library, primary hits were counter-screened in a *CMV-promoter-EGFP*-reporter assay and confirmed hits were further validated in dose–response curves and independent assays (Supplementary Fig. 3b–d). The main criteria for hit compound selection were the absence of immediate overall cell toxicity at 72 h of treatment and modulation of the KDM5B-promoter-driven expression of EGFP (abbreviated K/EGFP, for more details see "Methods"). Compounds that directly increased K/EGFP signals were not considered because of possibly masking effects by passive enrichment for KDM5B^{high} cells as previously seen for various cytotoxic drugs[5]. Instead, K/EGFP signal decrease was of particular interest because it could indirectly indicate a persistent increase of the endogenous KDM5B protein level as a result of chemical compound treatment (for example, through negative feedback of high KDM5B protein levels on mRNA transcription).

As confirmed by flow cytometric analysis and by immunocytology, the top hit compound 2-phenoxyethyl-4-(2-fluorophenyl)-2,7,7-trimethyl-5-oxo-1,4,5,6,7,8-hexahydroquinoline-3-carboxylate (PubChem name BAS00915510, here abbreviated Cpd1) reproducibly increased KDM5B protein levels irrespective of the genotype of the melanoma cell lines tested (Fig. 1e, f and Supplementary Table 1). A structurally homologous compound that failed to change K/EGFP transcription and endogenous KDM5B protein levels was selected as negative control for subsequent experiments (abbreviated Neg4, Supplementary Table 1 and Supplementary Fig. 3c, d). KDMs are histone demethylases and transcriptional regulators and as such mainly function in the nucleus[18–22]. Accordingly, quantitation of the KDM5B expression localization in nuclear vs. cytoplasmic compartments confirmed a Cpd1 time-dependent increase of nuclear KDM5B (Supplementary Fig. 3e) phenocopying the effect of Tet-On 3G-induced expression of KDM5B. Again, this was independent of the melanoma cell type tested (Supplementary Fig. 3f).

Due to the pronounced nuclear enrichment of KDM5B seen across the majority of melanoma cells upon Cpd1 treatment (Fig. 1f), we hypothesized that Cpd1 might affect the natural homeostasis of KDM5B protein as a potential mode of action. Longitudinal treatment of melanoma cells with the protein synthesis inhibitor cycloheximide revealed a steady decrease of KDM5B protein yielding a 79 and 98% decrease after 24 and 72 h, respectively. Co-treatment with Cpd1 resulted in an elevated
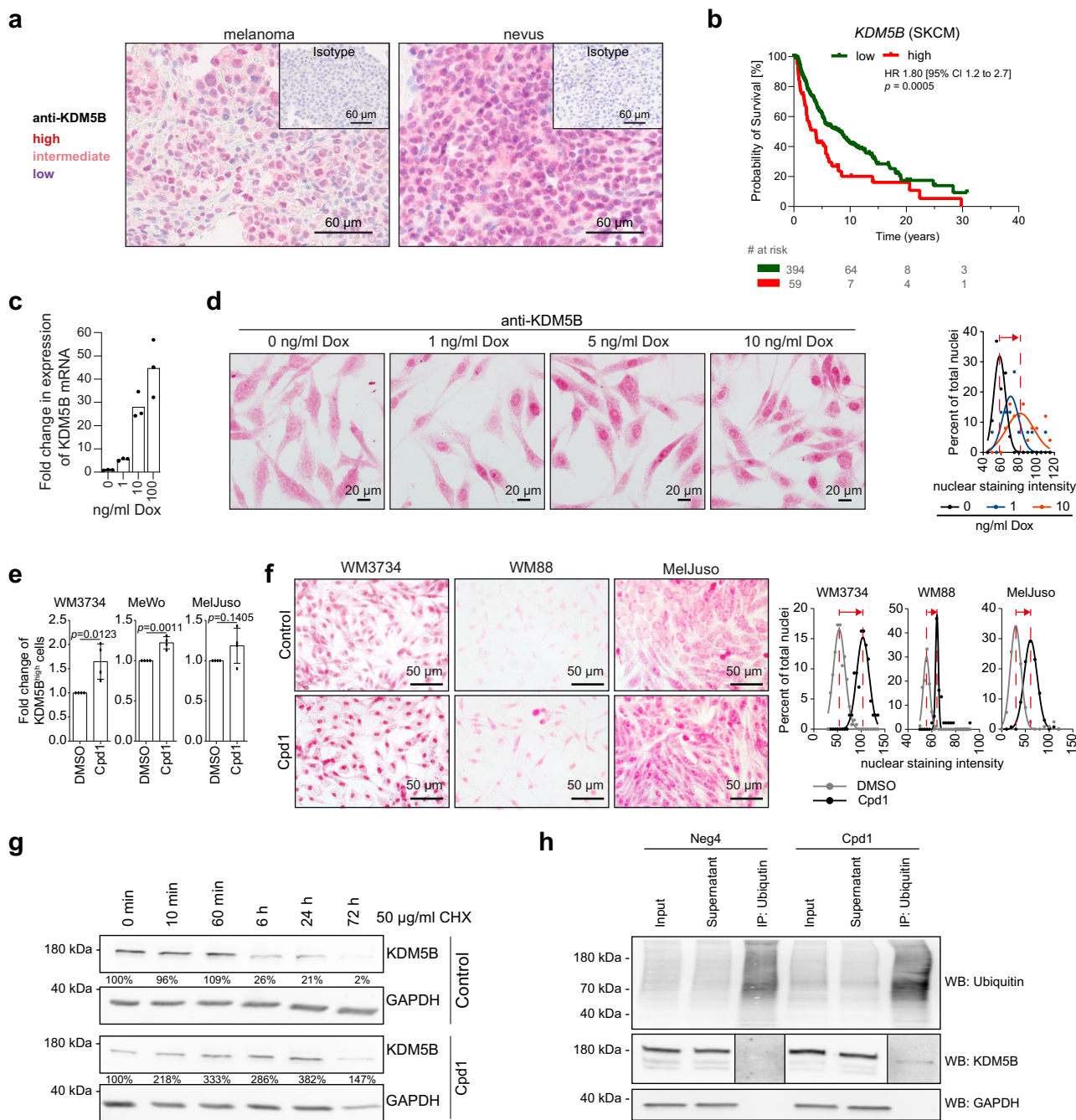
Fig. 1 Expression modulation of the histone H3K4 demethylase KDM5B/JARID1B. a Anti-KDM5B immunostaining of a melanoma patient sample (left) compared to a benign human nevus (right). Highly positive nuclei are dark red, medium positive nuclei are light red, low expressing nuclei are blue. Isotype controls are shown in the upper right corners. Depicted are representative images of different melanoma or nevi samples ($n = 5$ each). **b** Kaplan–Meier survival curves of cutaneous melanoma patients were calculated from the TCGA data set based on cut-point optimization for KDM5B expression (high expression, red, vs. low, green, TCGA browser tool UCSC Xena and GraphPad Prism). Sample sizes are indicated in the patient at risk table (# of risk). Significance was tested by Long-rank (Mantel–Cox) test. **c** Quantitation of KDM5B mRNA induction after 24 h of doxycycline (Dox) treatment as assessed by qPCR. Shown is one representative example (mean, $n = 2$). **d** Anti-KDM5B nuclear immunostaining of WM3734$^{Tet3G-KDM5B}$ cells after Dox-titration at the indicated concentrations for 24 h (left, representative images; right, quantitation shown as normalized frequency distribution of nuclear staining intensity). Shown is one representative out of three clones. **e** Flow cytometric detection of endogenous KDM5B protein levels after treatment with Cpd1 for 72 h. Mean ± SD ($n = 4$); two-sided *t*-test. **f** Anti-KDM5B nuclear immunostaining of three different melanoma cell lines (WM3734, WM88, MelJuso) after 72 h of 10 μM Cpd1 treatment (left, representative pictures; right, quantitation shown as normalized frequency distribution of nuclear staining intensity). **g** Time course of KDM5B protein levels after treatment of WM3734 cells with Cpd1 (10 μM) plus cycloheximide (CHX, 50 μg/ml, $n = 2$). **h** Ubiquitin protein conjugates were immunoprecipitated in WM3734 cells after Cpd1 treatment for 72 h. The total ubiquitinated cellular protein content was detected by a pan-ubiquitin-HRP antibody (upper row). The fraction of ubiquitinated KDM5B protein was detected by a KDM5B-specific antibody (middle row). Neg4 was used as structure homolog compound control ($n = 2$). To improve visualization of the KDM5B bands resulting from immunoprecipitation, the contrast was enhanced for both treatments equally. Source data are provided as a Source Data file.

KDM5B level (382 and 147% at 24 and 72 h), suggesting that Cpd1 might attenuate KDM5B protein degradation and by this maintain its nuclear expression level (Fig. 1g). To study the cellular degradation pathway of KDM5B, we established a proteolysis targeting chimera (PROTAC) model[23,24] (Supplementary Fig. 4a). This model is based on the binding of SLF′-thalidomide to FKBP12-tagged KDM5B. SLF′ is a synthetic binding ligand of FKBP12, while thalidomide recruits the E3 ubiquitin ligase cereblon for ubiquitination and subsequent proteosomal degradation of targeted KDM5B. Applying SLF′-thalidomide to FKBP2-tagged KDM5B in WM3734 melanoma cells, we could demonstrate that KDM5B protein is quickly proteosomally degraded in an E3 ubiquitin ligase-dependent manner (Supplementary Fig. 4b). Since proteasomal degradation is a calcium-dependent process[25,26] and the dihydropyridine structure of Cpd1 indicates a function as calcium channel blocker, we tested if Cpd1 affects the intracellular calcium content and the degradation level of ubiquitinated protein in melanoma cells. Indeed, both acute and long-term Cpd1 treatments led to a significant reduction in the store-operated calcium entry (Supplementary Fig. 4c) paralleled by an accumulation of ubiquitinated KDM5B (Fig. 1h).

Enforced expression of KDM5B directs melanoma cells towards a slow-growing persister state. Standard proliferation (MTT) and apoptosis (caspase 3 plus annexin V measurement or 7AAD flow cytometry) assays indicated a rather cytostatic than apoptotic or toxic effect in short-term Cpd1-treated melanoma cell lines or WM3734$^{Tet3G-KDM5B}$ cells (Fig. 2a, left panel and Supplementary Fig. 5a, b). For Cpd1, a maximum feasible dose of 10 μM was assumed based on cross-cell line comparisons in MTT assays (Supplementary Fig. 5c) and was used for all following experiments. In congruence with reports on KDM5B-associated therapy persistence[5,16,17], we observed decreased drug susceptibility to MAPK signaling pathway inhibitor (MAPKi) treatment upon KDM5B upregulation irrespective of the melanoma cell line tested (Fig. 2a, right panel).

Next, we tested how melanoma cell populations behaved, when the KDM5B expression spectrum was constantly directed to a higher level without the chance to dynamically revert to normal heterogeneity. Enforced expression of KDM5B in the WM3734$^{Tet3G-KDM5B}$ model reduced cell numbers in long-term two-dimensional (2D) growth assays and decreased anchorage-independent 3D-colony formation in a dose-dependent manner (Fig. 2b, c and Supplementary Fig. 5d). Growth of naïve WM3734 and WM3734$^{Tet3G-EGFP}$ control cells was not affected by doxycycline (Supplementary Fig. 5e). The KDM5B-mediated effect on tumor proliferation was then studied in vivo. We allowed xenografted WM3734$^{Tet3G-KDM5B}$ cells to establish tumors up to approximately 150 mm^3 before doxycycline was supplemented to the drinking water. This led to a significant tumor growth delay over nearly 2 weeks (Fig. 2d; $p < 0.05$, linear mixed-effect model).

Long-term treatment with Cpd1 significantly reduced the growth of different melanoma cell lines irrespective of their genotype (Fig. 2e, Supplementary Fig. 6a–c show examples for treatment up to 16 days). Also, melanoma cells that had previously developed resistance to MAPK inhibition responded to chemical enforcement of the KDM5B phenotype supporting the observation that chronically drug-resistant melanoma cell populations re-establish normal KDM5B heterogeneity after initial KDM5B enrichment (Fig. 2f and Supplementary Fig. 6d–g). 7AAD staining suggested that this effect is more the result of the antiproliferative effect of upregulated KDM5B than of compound toxicity (Supplementary Fig. 6h).

In addition, limited dilution assays and 3D-colony formation indicated a loss of tumor repopulation properties of melanoma cells under constant exposure to Cpd1 (Fig. 2g, h). In contrast, pre-treatment of melanoma cells with Cpd1 for only 3 days before seeding onto soft agar was not sufficient to reduce the number of formed colonies again suggesting spontaneous reversibility of the KDM5B phenotype under normal conditions (Fig. 2i and Supplementary Fig. 6i). Continuous treatment with Cpd1 also reduced the invasive capacity of melanoma cells in a 3D-collagen spheroid model (Fig. 2j). Interestingly, Cpd1 strongly impaired the capacity of melanoma cells to form proper spheroids; especially when treatment commenced before collagen embedding (Fig. 2k).

Finally, we tested Cpd1 in a xenograft and an immunocompetent syngeneic mouse melanoma model[5,27]. The phenotypic effects of Cpd1 treatment were confirmed beforehand in orthogonal in vitro assays for the murine CM cells, same as for the WM3734 cells (Supplementary Fig. 6j, k, Fig. 1e, f and Supplementary Figs. 3d, 5c, 6b, c, respectively). In both mouse models, Cpd1 treatment resulted in a significant antitumor growth effect in comparison to the vehicle control (Fig. 2l, m). Ex vivo immunostaining confirmed a Cpd1-induced shift towards high KDM5B expression states (Supplementary Fig. 6l).

In sum, our results suggest that KDM5B expression dynamics can be limited by exogenous genetic or chemical modulation providing a possibility to manipulate KDM5B-dependent tumor maintenance.

KDM5B-mediated cell cycle arrest and inhibition of cytokinetic abscission. Although persister cells have been repeatedly described to be slow-cycling in various cancer entities[4,6,9], their true cellular identity and proliferation phenotype remains elusive in melanoma. We first demonstrated by DNA content cell cycle analyses that enforced KDM5B expression over 72 h dose-dependently induces cell cycle delay across various genetically different melanoma cell lines (Fig. 3a and Supplementary Fig. 7a). Interestingly, time-lapse cell cycle imaging of single FUCCI-WM164 cells[28] revealed that Cpd1 treatment increases the total cell cycle length by 43.8% compared to DMSO- and Neg4 controls due to longer time spent in both G1 and S/G2/M phases (Fig. 3b and Supplementary Fig. 7b, c). Longitudinal DNA content cell cycle analysis under continuous treatment with Cpd1 up to 7 days (Neg4 as negative control) demonstrated that the Cpd1-induced delays of G1 and G2/M can occur in a temporally consecutive manner (Supplementary Fig. 7d). In sum, these experiments underscore the role of heterogeneity and temporal plasticity for effect size measurements across single melanoma cells, especially for the interpretation of phenotypic cell cycle readouts from single time points.

To further unravel the molecular mechanisms underlying the antiproliferative effect of KDM5B, we performed single-cell time-lapse microscopy of Cpd1-treated WM3734 cells vs. Neg4-treated control cells (Supplementary Movies 1–3). The quantitation of cell numbers after 72 h confirmed a reduction in cell proliferation (Fig. 3c). Interestingly, we observed that some cells undergoing cell division showed a prolonged time to complete cell abscission (Fig. 3d). We hypothesized that this phenomenon may be caused by a so far unknown regulatory role of KDM5B in cytokinesis (final process of physical separation of dividing cells). We aimed to quantitate this by immunostaining of intercellular midbodies, i.e. structures that represent microtubule-rich membrane bridges that connect two daughter cells shortly before their membranes fully dissever[29]. Indeed, we found a significant increase in the number of midbodies in a fraction of Cpd1-treated WM164 cells ($p \leq 0.0001$) as well as doxycycline-treated WM3734$^{Tet3G-KDM5B}$
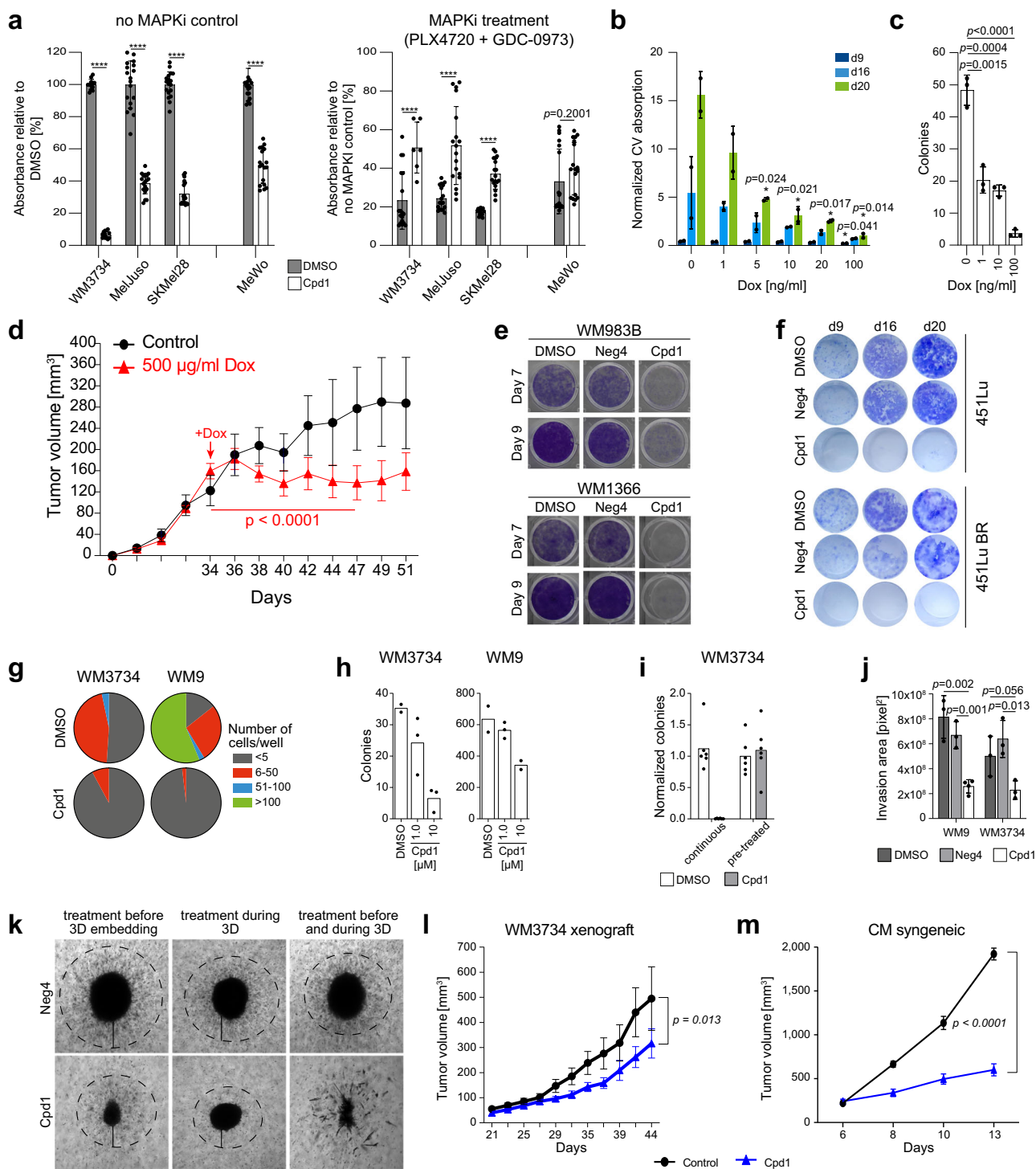
cells ($p = 0.0033$) (Fig. 3e). Importantly, the Cpd1-mediated increase of midbodies was rescued by SLF′-thalidomide-induced degradation of KDM5B in WM3734$^{Tet3G-KDM5B-FKBP12}$ cells (Fig. 3f). Transcriptional and proteomic profiling of KDM5B-enforced WM3734 cells by RNAseq and label-free quantitative mass spectrometry after 72 h of 10 μM Cpd1 revealed a small overlap of 11 genes/proteins, of which 7 have known functions during cytokinesis (Fig. 3g and Supplementary Data 1 highlighted in bold). For example, *AURKB, MKI67, KIF4A, UBE2C, RRM2, KIF1C1*, and *ANLN* are attributed to the GO cytoskeleton-dependent cytokinesis. For the expression of a subset of genes (*AURKB, KIF4A, SHCBP1*, and *UBE2C*), we found a

downregulation in both Cpd1-treated WM3734 as well as doxycycline-treated WM3734$^{Tet3G-KDM5B}$ cells (Fig. 3h). *AURKB, KIF4A*, and *UBE2C* are known to regulate spindle assembly and coordinate abscission[30,31]. *SHCBP1* is involved in midbody organization and cytokinesis completion[32]. Thus, irrespective of the model used, the above-mentioned genes may be functionally involved in the observed increase in midbodies and the delay in cell doubling.

Our experiments suggest so far that exogenous expression of KDM5B can direct melanoma towards a slow-cycling tumor phenotype across the majority of tumor cells, where different molecular mechanisms might cooperate to prevent cell

Fig. 2 In vitro and in vivo effects of enforced KDM5B expression. a MTT assays with Cpd1 started at day −7, and then MAPKi was added for 72 h. Readout after 72 h of MAPKi (5 μM PLX4720 + 0.5 μM GDC-0973) and in total 10 days of Cpd1. Cell numbers after 10 days of DMSO or Cpd1 without MAPKi (left panel) and after 72 h of MAPKi compared to "no MAPKi control" (right). Mean ± SD ($n = 3$), two-sided t-test (****$p \leq 0.0001$). **b** Clonogenic growth after KDM5B induction (9, 16, and 20 days). Mean ± SD, two-sided t-test. Shown is one out of six clones. **c** Soft agar colony formation after 52 days of KDM5B induction. Shown is one representative experiment ($n = 3$). Mean ± SD; two-sided t-test. **d** Growth of xenografted WM3734$^{Tet3G-KDM5B}$ cells. Doxycycline treatment started day 34. Mean ± SEM with $n = 6$ mice in the control and $n = 10$ mice in the treatment group, linear mixed-effect spline model. **e** Clonogenic growth assay of WM983B and WM1366 cells continuously treated over 7 and 9 days with 10 μM of Cpd1 or Neg4 ($n = 3$). **f** Clonogenic growth assay of 451Lu and resistant 451Lu BR cells treated over 9, 16, and 20 days with 10 μM of Cpd1 vs. DMSO or Neg4 controls ($n = 2$). **g** Two-dimensional colony formation after continuous treatment with 10 μM Cpd1 for 19 days. Mean, $n = 3$. **h** Soft agar colony formation under constant Cpd1 treatment at the indicated doses over 30 days (one representative experiment out of $n = 2$) and **i** compared to short-term treatment for 72 h before seeding without treatment continuation (mean, $n = 2$). **j** Collagen invasion of WM3734 spheroids under 10 μM of Neg4 or Cpd1 at day 10. Shown is one representative experiment ($n = 3$). Mean ± SD; two-sided t-test. **k** WM3734 melanoma spheroids at day 10 after collagen embedding. **l, m** Growth of xenografted WM3734 cells (left, $n = 9$ mice per group) and syngeneic CM cells (right, $n = 3$ per control and $n = 5$ mice per treatment group). Cpd1 treatment was started when tumors were palpable. Mean ± SEM, linear mixed-effect spline model. Source data are provided as a Source Data file.

proliferation. Regarding potential clinical implications, reducing persister state plasticity could provide a therapeutic gain in time by delaying tumor progression. However, this approach might be more effective, if slow-cycling and potentially tumor repopulating persister states are additionally eradicated by exploiting state-specific drug sensitivities.

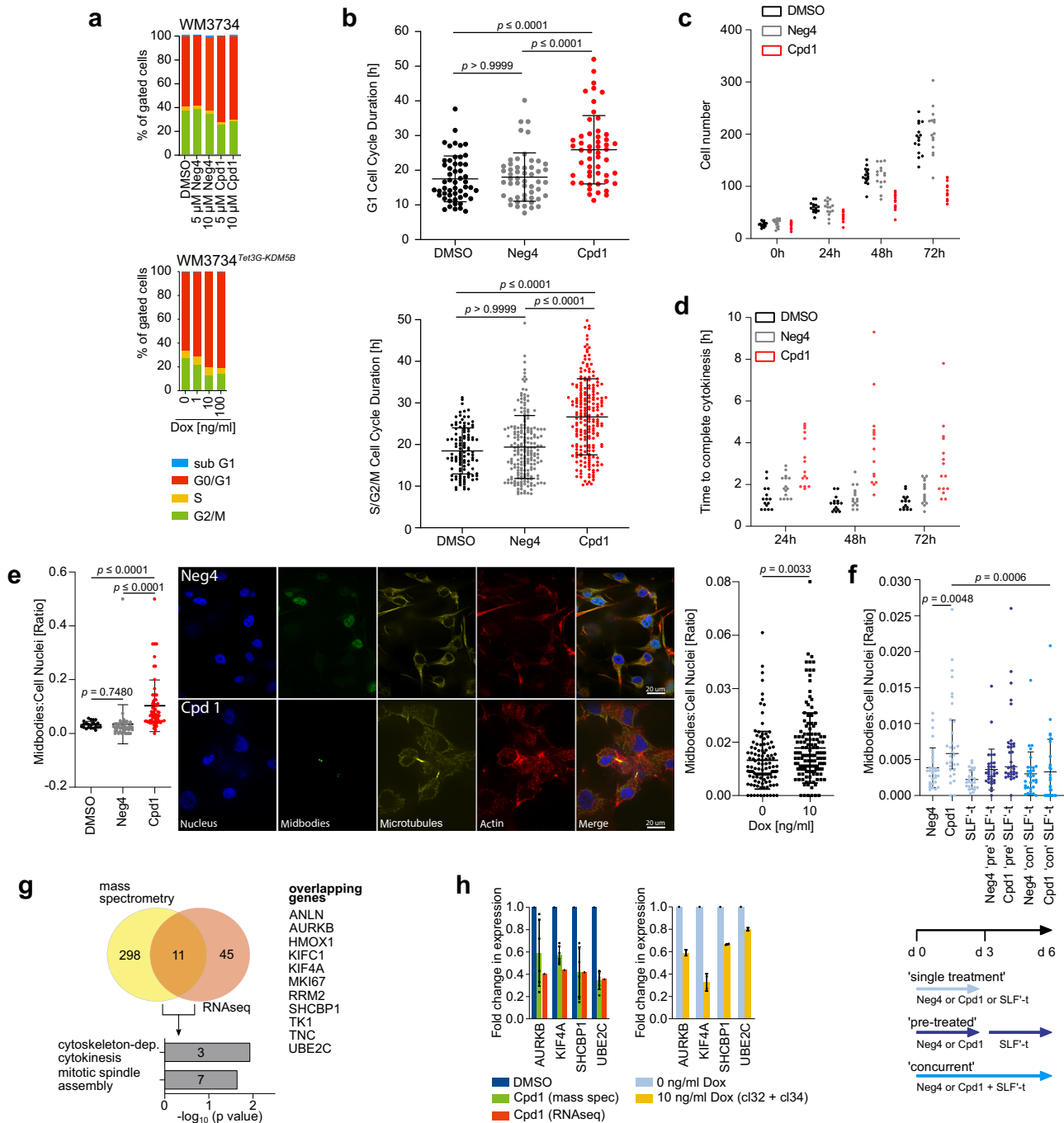**Enforced KDM5B expression leads to lineage reprograming.** To unravel potential changes in cellular identity and underlying transcriptional programs after enforced KDM5B expression, we performed RNA sequencing of our genetic and chemical KDM5B induction models (Tet-On 3G and Cpd1) head-to-head. WM3734$^{Tet3G-KDM5B}$ cells were treated for 24, 48, and 72 h with doxycycline and then harvested for analysis. In parallel, naïve WM3734 and patient-derived short-term cultured CSM152 cells were treated with Cpd1 and analyzed after 72 h (Supplementary Data 2). We first checked if Cpd1 also transcriptionally phenocopies the effect of Tet-On 3G-mediated KDM5B induction. Indeed, we found that both of our models can regulate a previously published KDM5B target gene motif (SCIBETTA_KDM5B_TARGETS_DN (DN = "down") motif, 79 genes) to a similar degree[21] (Supplementary Fig. 8a). Subsequent Gene Set Enrichment Analysis (GSEA) followed by Cytoscape visualization revealed a transcriptional landscape that matched other expected KDM5B-associated pathways like chromosomal remodeling or ATP-ase metabolism. Also, genes involved in cell cycle/mitosis, DNA damage response, RNA processing, and immune response were found to be regulated by KDM5B (Supplementary Fig. 8b). Transcripts that control cell cycle and mitosis revealed a steadily increasing and statistically significant regulation from 24 to 48 and 72 h of KDM5B induction pointing to a fundamental and temporally dynamic influence on the cell proliferation machinery (Supplementary Fig. 8c).

As KDM5B has been reported to guide developmental processes in a highly conserved fashion[33–35], we asked if enforced KDM5B expression could affect the differentiation state of melanoma cells. Indeed, we observed for genetic as well as chemical KDM5B enforcement an impressive downregulation of mesenchymal (SARRIO_EPITHELIAL_MESENCHYMAL_TRANSITION_DN, 145 genes)[36] and proliferative (GERBER_PROLIFERATION_SPOT A, 405 genes)[37] gene motifs (Fig. 4a, FWER $p < 0.05$ was considered as statistically significant). Additionally, melanocytic differentiation genes were specifically regulated in both models (GO_PIGMENTATION[38,39], 86 genes, Fig. 4b). Most strikingly, enforced KDM5B expression was followed by a time-dependent transcriptional shift, in which cells were gradually transitioning from undifferentiated and neural crest-like to transitory-melanocytic and melanocytic gene motifs over time (Fig. 4c and Supplementary Table 2). Accordingly,

KDM5B knockdown showed an inverse gene expression towards undifferentiated states (Fig. 4c, control WB in Supplementary Fig. 8d). In an independent control experiment, differentiation reprograming was reproduced for Cpd1 and occurred also in a time-dependent manner (Supplementary Fig. 8e, Supplementary Table 2 and Supplementary Data 3). Importantly, KDM5B-associated differentiation reprograming was similarly induced by Cpd1 in patient-derived CSM152 melanoma cells (Fig. 4a, b and Supplementary Fig. 8a, e) and was also confirmed in silico for endogenous gene expression in single melanoma cells isolated from human tumor tissue ($n = 1253$ melanoma cells from 19 tumors[40]). Here, KDM5B expression was significantly higher in cells with melanocytic gene signatures compared to cells with undifferentiated signatures (Fig. 4d).

KDM5B is an epigenetic determinant of cytokinesis and differentiation gene transcription. Considering KDM5B's known role as a histone demethylase with direct involvement in transcriptional regulation, we performed an in silico analysis of KDM5B and H3K4me3 ChIP-Seq data using the ChIP-Atlas[41] set to "all cell type class" as well as H3K4me3 ChIP-Seq data from breast cancer[42] and melanoma cells[43,44]. This suggested a correlation between KDM5B DNA-binding motifs and H3K4me3 chromatin marks across a number of cytokinesis genes (breast cancer and melanoma cell lines) and melanocytic differentiation genes (melanoma cell lines) (Fig. 5a, b). Specifically, this included the cytokinesis genes *AURKB*, *KIF4A*, *SHCBP1*, and *UBE2C* as well as the differentiation genes *MITF*, *MLANA*, *NGFR*, *AXL*, *TYR*, *TJP1*, *CDH2*, *ZEB1* and *SMAD1*, which we showed to be regulated in a Cpd1-dependent manner (Figs. 3g, h and 4a–d).

To functionally support that the observed effects of Cpd1 on gene expression are truly KDM5B-dependent, we have performed siRNA knockdown of KDM5B and subsequently measured transcriptional expression of selected cytokinesis and differentiation genes upon concurrent Cpd1 treatment (Fig. 5c, d). As expected, cytokinesis genes, which we have found downregulated after genetic (and Cpd1-mediated) KDM5B upregulation in Fig. 3h, were upregulated at mRNA level after siRNA knockdown of KDM5B as compared to the scrambled control (e.g., AURKB, KIF4A, Fig. 5d, Neg4 treatment). Accordingly, differentiation genes, which we found to be upregulated upon KDM5B induction (Fig. 6a), were downregulated after KDM5B knockdown. When we treated with scrambled control cells with Cpd1, we again saw the expected downstream effects of KDM5B induction, i.e., mRNA downregulation of cytokinesis and upregulation of differentiation genes (gray bars). When we added Cpd1 to cells with siRNA KDM5B knockdown, Cpd1 could not maintain the KDM5B protein level (Fig. 5c, no KDM5B protein was produced that could be preserved from proteasomal degradation) and,

Fig. 3 KDM5B-mediated cell cycle arrest and inhibition of cytokinetic abscission. a Propidium iodide cell cycle analysis of Cpd1-treated WM3734 (above) or Dox-treated WM3734$^{Tet3G\text{-}KDM5B}$ cells (below) after 72 h. Shown are representative data ($n = 4$). **b** Quantitation of the G1 (upper panel) and S/G2/M (lower panel) cell cycle duration by real-time cell cycle imaging of FUCCI-WM164 cells pretreated with Cpd1 (10 µM) vs. DMSO or Neg4 controls (10 µM) for 72 h. Scatter dot plots represent mean ± SD ($n = 3$); Kruskal–Wallis test. **c** Time-lapse imaging analysis of WM3734 cell numbers during treatment with Cpd1 (10 µM) vs. DMSO or Neg4 controls (10 µM) up to 72 h (15 different areas, $n = 2$). **d** Time-lapse microscopic movies were analyzed for the time to complete cytokinesis (15 different cells, $n = 2$). **e** Quantitation and representative immunofluorescence staining of midbodies in Cpd1-treated (72 h) WM164 cells (left) and Dox-treated WM3734$^{Tet3G\text{-}KDM5B}$ cells (right) vs. respective controls. Depicted are single fluorescence channels: blue (DAPI, nucleus); yellow (α-tubulin, microtubules); green (Aurora B kinase, midbodies); red (phalloidin, F-actin). Dot plots show the ratio of midbodies/cell per field of view, 12–16 fields, $n = 3$. Mean ± SD, left, one-way ANOVA: right, two-sided t-test. **f** Quantitation of midbody decrease in the KDM5B-PROTAC model. Proteasomal degradation of KDM5B was induced by SLF′-thalidomide (SLF′-t) concurrently applied with Cpd1 ("con") or applied after Cpd1 pre-treatment for 3 days ("pre"). Neg4 was used as control. Dot plots show the ratio of midbodies/cell nuclei as median values with the interquartile range (4 coverslips, $n = 2$; one-way ANOVA). **g** Venn diagram and gene ontology analysis of significantly regulated genes upon Cpd1 (10 µM) treatment of WM3734 cells as detected by mass spectrometry and RNA sequencing. **h** Quantitation of downregulation of selected cytokinesis regulators as assessed by mass spectrometry and RNAseq (left, $n = 1$) or qPCR (right, mean ± SD, $n = 2$) in Cpd1-treated WM3734 and Dox-treated WM3734$^{Tet3G\text{-}KDM5B}$ cells. Source data are provided as a Source Data file.
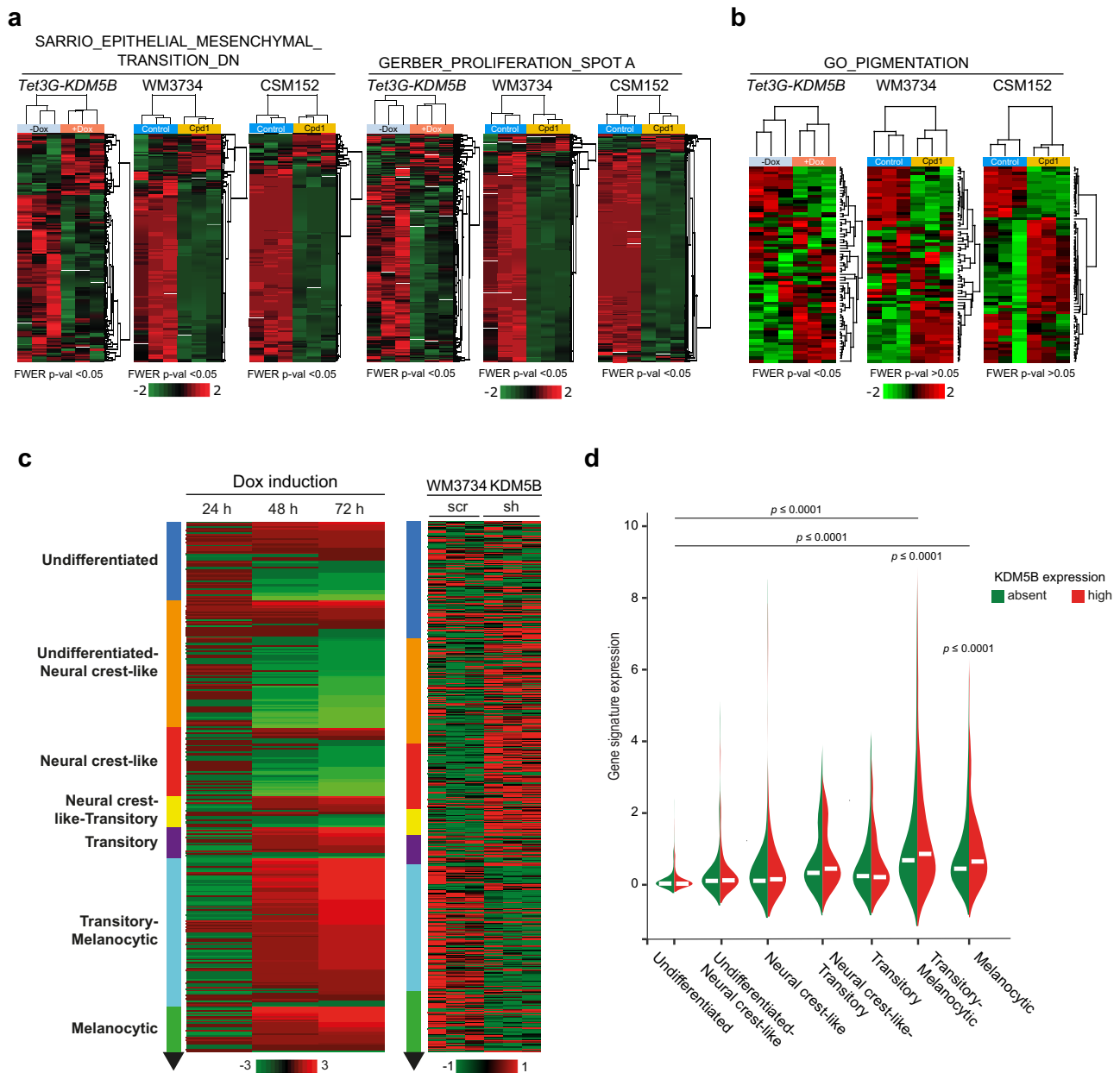
Fig. 4 KDM5B leads to a differentiation-directed phenotypic shift. a, **b** Heatmaps of the SARRIO_EPITHELIAL_MESENCHYMAL_TRANSITION_DN[36], GERBER_PROLIFERATION_SPOT A signatures[37] (**a**) and GO_PIGMENTATION signature[38,39] (**b**) from WM3734^(Tet3G-KDM5B) cells after 72 h of Dox treatment and WM3734 and CSM152 cells after 72 h of Cpd1 treatment; red, upregulated; green downregulated genes. Significance is indicated by FWER $p < 0.05$. **c** Heatmap of the Tsoi differentiation trajectory[66] for WM3734^(Tet3G-KDM5B) cells after 24, 48, and 72 h Dox treatment (left), WM3734 KDM5B knockdown (sh) versus control (scr) cells (right); red, upregulated, green downregulated genes. **d** Violin plot displaying endogenous KDM5B expression levels according to the transcriptional differentiation level in single-cell RNA-sequenced human melanomas. Asterisks represent a p value <0.0001 from one-way ANOVA with Dunnett's multiple comparison test. Here the comparison was made to the undifferentiated group.

consequently, could not reverse siRNA-dependent regulation of KDM5B downstream genes (white bars).

Enforced KDM5B expression leads to lineage-directed vulnerability. The observed KDM5B-dependent cell state reprograming not only confirms commitment to melanocytic differentiation, it could also sensitize melanoma cells for secondary phenotype-specific drugs. We sought to take advantage of 3-O-(3,4,5-tri-methoxybenzoyl)-(−)-epicatechin (TMECG), a tyrosinase (TYR)-processed antimetabolic agent previously described to eliminate melanoma cells in a lineage-specific way[45]. Thus, we first assessed whether Cpd1 treatment truly activates the melanocytic

differentiation/pigmentation machinery in melanoma cells. Indeed, we found a significant time-dependent Cpd1-induced transcription of the melanocytic master regulator *MITF* and other downstream differentiation genes like *DCT, TYR*, and *MART-1/MLANA* in pigmentation-competent melanoma cells (Fig. 6a). Conversely, knockdown of KDM5B was associated with a decrease in differentiation gene expression (Fig. 6b). Immunoblotting of WM3734^(Tet3G-KDM5B) cells confirmed a KDM5B-dose-titratable increase of MITF protein, whereas typical markers of mesenchymal cell phenotypes such as CDH2, AXL, ZEB1, or SMAD1 proteins were decreased (Fig. 6c). A similar tendency of regulation of these markers at protein level was confirmed for
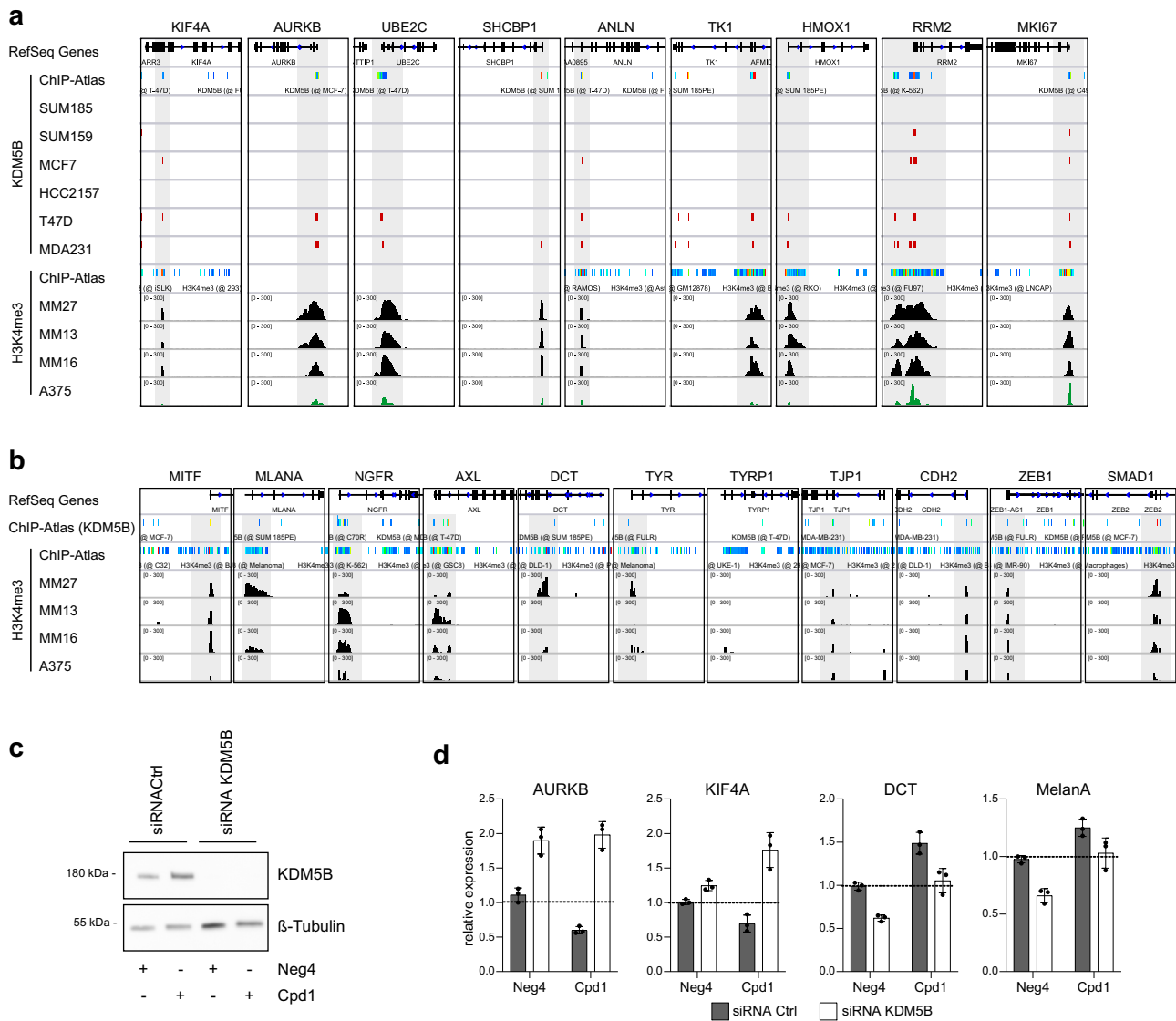
Fig. 5 KDM5B-dependent cytokinesis and differentiation gene transcription. In silico analysis of cytokinesis and mitotic spindle assembly genes (**a**) or differentiation genes (**b**) of KDM5B- and H3K4me3-ChIPseq data from breast cancer cell lines SUM185, SUM159, MCF7, HCC2157, T47D, and MDA231 (GSE46073[42]) and melanoma cell lines MM27, MM13, MM16 (GSE71854[44]) and A375 (GSE99835[43])) and ChIP-Atlas[41]. **c** KDM5B knockdown in MaMel63a cells was confirmed by immunoblotting 4 days after siRNA transfection. **d** KDM5B target gene expression of cytokinesis-related genes (AURKB, KIF4A) and differentiation-related genes (DCT, MelanA) was analyzed by qPCR 4 days after KDM5B knockdown and 3 days of Neg4 or Cpd1 treatment (10 µM). Shown is one representative example (mean ± SD, $n = 2$). Source data are provided as a Source Data file.

Cpd1 (Fig. 6d). Lastly, immunostained sections from syngeneic melanomas after Cpd1 treatment (Fig. 2m) confirmed enriched MITF protein expression in vivo (Fig. 6e, upper row). Fontana-Masson staining additionally indicated a focal increase of intracellular melanin production (Fig. 6e, lower row).

We next tested lineage-directed melanoma cell sensitization by Cpd1 in preclinical models. We tested combinations of Cpd1 with TMECG in three melanoma cell lines in vitro (WM3734, MaMel63a, WM983B, Fig. 6f and Supplementary Fig. 9). MTT assays revealed that TMECG in combination with Cpd1 was more effective in cells, which were pretreated with Cpd1 for 3 days. This complemented our prior observation that KDM5B-directed cell reprograming towards cell differentiation is a time-dependent process (Fig. 4c and Supplementary Fig. 8e). TMECG alone showed a limited effect on cell numbers and, therefore, was defined next to Cpd1 as mono-treatment control for subsequent in vivo combination therapies (Fig. 6g). The effect of Cpd1 alone on in vivo tumor growth compared to

vehicle control was assessed beforehand (Fig. 2l). To study the influence of the temporal sequence of TMECG and Cpd1 in vivo, we set up a therapy model, in which WM3734 cells were xenografted to establish tumors on the back of immunodeficient NMRI-(nu/nu)-nude mice over 20 days (Fig. 6g, left). Co-treatment of Cpd1 and TMECG was started either simultaneously or consecutively, i.e., the tumors were pretreated with Cpd1 for one week before TMECG was added. In line with our in vitro observations, melanoma tumor growth was significantly reduced when established tumors were primed to differentiation before state-specific elimination started (Fig. 6g, right; $p < 0.05$, Mann–Whitney test). Concurrent treatment of Cpd1 and TMECG failed to reduce tumor size within the time span of our animal protocol. A possible long-term effect of Cpd1 also in the concurrent setting could not be assessed in this model.

To summarize, our study provides proof-of-concept for a dual hit strategy in melanoma, in which persister state-directed
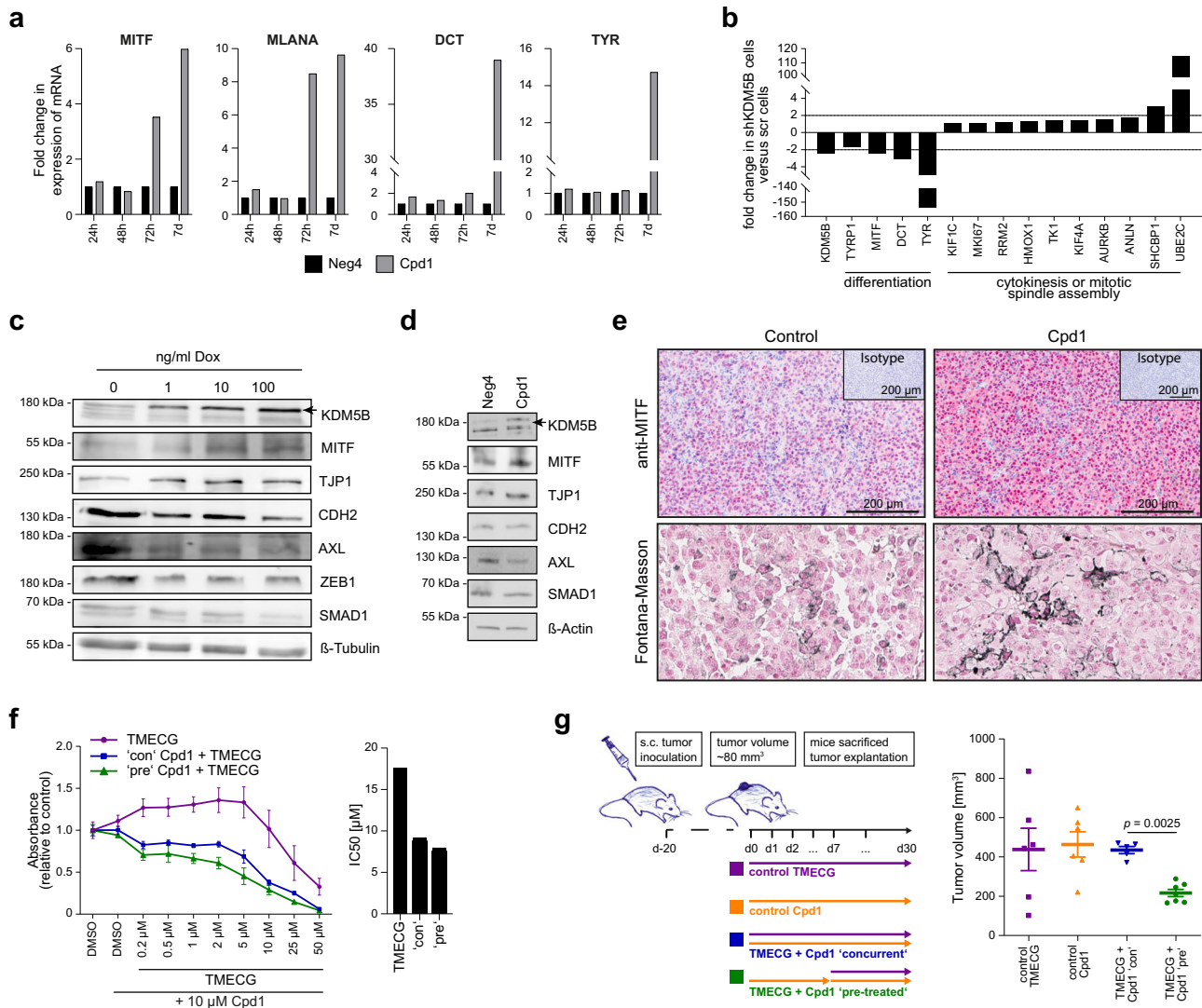
Fig. 6 Enforced KDM5B expression facilitates melanocytic lineage-directed elimination by TMECG. a Quantitation of mRNA after 24 h, 48 h, 72 h and 7 days of Cpd1 treatment of MaMel63a cells as assessed by qPCR. Mean ± SD. Shown is one representative example. **b** Regulation of differentiation, cytokinesis, and mitotic spindle assembly genes as detected by cDNA microarray analysis after KDM5B shRNA knockdown in WM3734 cells ($n = 1$). **c, d** Immunoblotting of melanocytic lineage and (de-)differentiation markers after 24 h of KDM5B induction in WM3734$^{Tet3G-KDM5B}$ cells (**c**) and after 72 h of Cpd1 treatment in MaMel63a cells (**d**). Shown are representative data ($n = 2$). **e** Anti-MITF immunostaining (upper panel) and Fontana-Masson staining (lower panels) of CM melanoma tumor grafts from Cpd1-treated vs. control mice. **f** MTT cell viability assay of WM3734 cells. Representative example is shown left (mean ± SD, $n = 2$) and corresponding IC$_{50}$ values on the right. TMECG was either concurrently given together with Cpd1 ("con") or added 3 days after Cpd1 pre-treatment ("pre"). Readout was performed after 72 h of TMECG treatment. **g** Persister-state-directed therapy model in vivo. Left: schematic representation of treatment dosing and timing in immunodeficient NMRI-(nu/nu)-nude mice. Right: tumor volumes of WM3734 xenografts (endpoint at day 30). TMECG was either concurrently given together with Cpd1 ("con") or added one week after Cpd1 pre-treatment ("pre"). Mean ±SEM (6 mice in TMECG and Cpd1 control group, five mice in "con" and seven mice in "pre" group). Significance was determined by two-sided Mann–Whitney test. Source data are provided as a Source Data file.
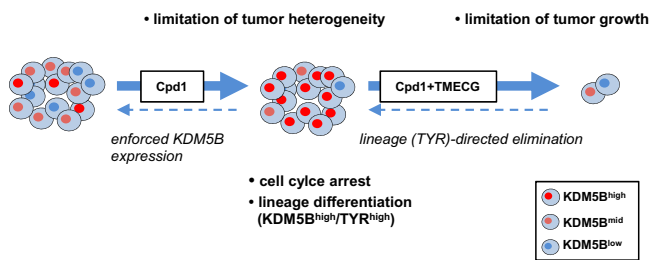

Fig. 7 Phenotype-specific dual hit strategy in melanoma. KDM5B persister state-directed transitioning limits tumor plasticity and heterogeneity and primes melanoma cells towards lineage-specific elimination.

transitioning limits cell state plasticity and primes tumor cells towards differentiation-specific elimination (Fig. 7).

Discussion

Next to genetic tumor evolution, particularly phenotypic cell plasticity is an emerging problem in cancer therapy[46]. As melanoma cells are rapidly shifting between different transcriptional, cell proliferation, and differentiation programs, such phenotypes may transiently overlap and rapidly adapt to any strategy that specifically attacks single drug resistance mechanisms[1–3,47]. Thus, one question of this study was if limiting phenotypic cell state dynamics could become a starting point for a dual hit strategy in

melanoma. The slow-cycling KDM5B^high melanoma cell phenotype was used as a model for proof-of-concept.

So far, the real nature of slow-cycling KDM5B^high persister cells in melanoma was unknown. Our data suggest that KDM5B directs the transcriptional identity of melanoma cells from undifferentiated towards melanocytic lineage differentiation. KDM5B-induction upfront to therapy changed the frequency of intrinsically resistant melanoma cells similar to the recently reported DOT1L-inhibited state[3]. Inhibition of the histone H3K79 methyltransferase DOT1L by gene knockout in a CRISPR-Cas9 screen favored a neural crest cell differentiation program (NGFR^high/EGFR^high state) and increased the number of cells primed to resistance upfront to BRAF inhibitor treatment. Future studies on single-cell transcriptional and proteomic level have to decipher, if KDM5B induction and DOT1L inhibition drive cellular identity towards the same end stage and how strong these effects depend on the actually active gene expression level and time required for phenotypic reprogramming.

In accordance with reports on KDM5B-dependent cell fate decisions and lineage commitment in other tissues types (e.g. neural differentiation[34] or hematopoiesis[48]), our study suggests that KDM5B acts as a highly dynamic coordinator of both differentiation and cell division programs in melanoma. We show that KDM5B efficiently suppresses cell proliferation via downregulation of genes, which control cytoskeleton-dependent cytokinesis like *AURKB*, *KIF4A*, *UBE2C*, and *SHCBP1*[30–32]. Our midbody analysis estimates that a considerable fraction of KDM5B-enforced melanoma cells needs prolonged time to complete cell abscission, which might contribute the observed overall cell cycle delay. As KDM5B is not affected by inactivating mutations in most melanomas according to currently available genetic profiling data like TCGA (mutation frequency of 5.9% according to CBioPortal), it may represent an ideal way for melanoma cells, irrespective of their mutational background to secure a slow-cycling state whenever required. Conceptually, this could mean that melanoma cells exploit the slow-cycling differentiated KDM5B^high state to immediately survive selective pressure, but must decrease KDM5B expression again and resume cell cycle progression in favor of more proliferative cell phenotypes to ensure long-term tumor repopulation (plasticity addiction).

Although we consider the KDM5B^high phenotype as differentiated, we are aware that any terminology that is applied to describe phenotypic cell states in melanoma needs to be used with caution because of their highly volatile nature. Under prolonged KDM5B induction, we observed changes in RNA signatures and protein marker profiles over time. Depending on the time point chosen for experimental read-out, marker constellations, or even functional behavior like cell proliferation can be misleading for assessment of whether a certain cell state is advantageous or disadvantageous for tumor cell survival or drug killing. In this regard, our results unveiled a "Janus-faced" role of the KDM5B^high melanoma cell state. On the one hand, melanoma growth and cell invasion are impaired, when the slow-cycling state is sustained. On the other hand, melanoma cells can exploit this state to immediately survive targeted or cytotoxic therapies. However, as demonstrated here, when KDM5B^high state-directed transitioning is combined with a state-specific elimination strategy (instead of unspecific debulking drugs), control of tumor growth is possible. In fact, multiple applications of cell state-directed elimination are conceivable now; particularly as a rescue strategy or to deepen response in residual disease after state-of-the-art cancer therapies. Thus, we plan to systematically test Cpd1/TMECG in sequential therapy regimens with other therapies in future studies ideally using a chemically improved version of Cpd1 with optimized solubility.

Methods

Melanoma cell lines, patient samples, and culture. The following human melanoma cell lines were maintained in 2% fetal bovine serum (FBS)-substituted (Tu2%[49]) plus 6.8 mM L-glutamine or 4% FBS-substituted (Tu4%[50] melanoma medium at 5% CO₂: Wistar cell lines 451Lu (*BRAF^V600E*, *PTEN^wt*, *NRAS^wt*), 451Lu BR (*BRAF^V600E*, *PTEN^wt*, *NRAS^wt*), WM164 (*BRAF^V600E*, *PTEN^wt*, *NRAS^wt*), WM3734 (*BRAF^V600E*, *PTEN^del*, *NRAS^wt*), WM88 (*BRAF^V600E*, *PTEN^wt*, *NRAS^wt*), WM9 (*BRAF^V600E*, *PTEN^del*, *NRAS^wt*), WM983B (*BRAF^V600E*, *PTEN^wt*, *NRAS^wt*), WM983B BR (*BRAF^V600E*, *PTEN^wt*, *NRAS^wt*). Details on WM3734^KDM5Bprom-EGFP, lentiviral infected WM3734_sh_KDM5B_62 and WM3734_sh_scramble control cells and WM3734^Tet3G-shJARID1B were previously described[15,51]. The commercial human melanoma cell lines MelJuSo (*BRAF^WT*, *PTEN^WT*, *NRAS^NRASQ61L*), MeWo (*BRAF^WT*, *PTEN^WT*, *NRAS^wt*), SKMel5 (*BRAF^V600E*, *PTEN^n.d.*, *NRAS^wt*), SKMel28 (*BRAF^V600E*, *PTEN^T167A*, *NRAS^wt*) were grown in RPMI medium with 10% FBS. The primary patient-derived melanoma cell lines CSM027 (*BRAF^V600E*, *PTEN^wt*, *NRAS^wt*), CSM152 (*BRAF^wt*, *PTEN^wt*, *NRAS^wt*), MaMel63a (*BRAF^V600E*, *PTEN^wt*, *NRAS^wt*), ES014028 fibroblasts and the murine melanoma cell line CM[27] were also grown in RPMI medium with 10% FBS. Resistance of 451Lu BR and WM983B BR was maintained by 1 μM PLX4720 (vemurafenib isoform[52]). For transient knockdown of KDM5B, siRNA vectors (Flextube, Qiagen) were transfected into melanoma cells using jetPRIME® according to the manufacturer's protocol. Studies on human tissue samples and establishment of human melanoma cell lines were approved by the Internal Review Boards of the University of Pennsylvania School of Medicine and The Wistar Institute or the ethics committees of the Medical Faculties of the University of Wuerzburg and the University of Duisburg-Essen (reference numbers: 123/08_ff, 11-4715, 17-7391-BO). Cells were harvested using trypsin/EDTA 0.05%/0.02% in phosphate-buffered saline (PBS) (Biochrom). Cell line identity was confirmed by PCR-based DNA fingerprinting at the Department of Pathology of the University Hospital Essen. Cell culture supernatants were routinely tested for mycoplasma contamination using PCR with mycoplasma-specific primers.

Establishment of an inducible Tet-On 3G-KDM5B and KDM5B-PROTAC model. A lentiviral Tet-On 3G-*KDM5B* construct was cloned for inducible KDM5B protein expression. Cloning steps were planned by VectorBuilder. The Tet-On transactivator protein is encoded by the *pLV-Hygro-CMV-Tet3G* vector. The TRE response vectors contain a P_TRE3G promoter followed by either the human *KDM5B* gene, transcript variant 1, NM_001314042.1 (subcloned from *pBIND-RBP2-H1* (ref. [53]) or, as control, the *EGFP* gene (*pLV-Puro-TRE3G-hKDM5B* and *pLV-Puro-TRE3G-EGFP*, respectively). In brief, WM3734 cells were stably infected with *pLV-Hygro-CMV-Tet3G* using JetPRIME Polyplus (NYC, NY, USA) according to the manufacturer's protocol. After selection by hygromycin B and single-cell cloning, WM3734^Tet3G cells were stably infected either with *pLV-Puro-TRE3G-hKDM5B* or *pLV-Puro-TRE3G-EGFP* followed by puromycin selection. Double-infected WM3734 melanoma cells (WM3734^Tet3G-KDM5B or WM3734^Tet3G-EGFP) were maintained in Tu2% media. For doxycycline-inducible expression of the exogenous KDM5B-FKBP12 fusion protein, a lentiviral expression vector was cloned based on pLV-Puro-TRE3G-hKDM5B and WM3734 cells infected and selected as described above. Endogenous KDM5B was genetically knocked-out in WM3734^Tet3G-KDM5B-FKBP12 cells by CRISPR/Cas9 following standard protocols[54]. E3 ligase-dependent degradation was induced by supplementing 1 μM SLF'-thalidomide to the culture medium according to published procedures[24].

Drugs and chemical compounds. The following drugs and compounds were used: ampicillin (AppliChem, Omaha, NE, USA), blasticidin (InvivoGen, San Diego, CA, USA), cisplatin (1 mg/ml solution, Teva, Petach Tikwa, Israel), cycloheximide (Sigma-Aldrich, St. Louis, MO, USA), DMSO (AppliChem, Omaha, NE, USA), doxycycline (AppliChem, Omaha, NE, USA), Fura-2 AM (Thermo Fisher Scientific GmbH, Schwerte, Germany), hygromycin (AppliChem, Omaha, NE, USA), MG132 (Sigma-Aldrich, St. Louis, MO, USA), the vemurafenib isoform PLX4720 (Selleckchem Houston, TX, USA), GDC-0973/cobimetinib (Selleckchem Houston, TX, USA), puromycin (Merck, Darmstadt, Germany), trametinib (Selleckchem Houston, TX, USA), Neg4 ((oxolan-2-yl)methyl-4-(6-bromo-2H-1,3-benzodioxol-5-yl)-2,7,7-trimethyl-5-oxo-1,4,5,6,7,8-hexahydroquinoline-3-carboxylate, Chem-Div, San Diego, CA, USA) and Cpd1 (2-phenoxyethyl 4-(2-fluorophenyl)-2,7,7-trimethyl-5-oxo-1,4,5,6,7,8-hexahydroquinoline-3-carboxylate, ChemDiv, San Diego, CA, USA). Neg4 and Cpd1 were dissolved in DMSO at a stock concentration of 10 mM and diluted 1:1000 in media. 3-O-(3,4,5-trimethoxybenzoyl)-(−)-epicatechin (TMECG) was synthesized as described previously[55] and was made available by JN Rodríguez-López.

Small chemical compound screening. To identify compounds which modulate expression levels of KDM5B in melanoma cells, a small-molecule library was screened using our previously published KDM5B-promoter-*EGFP* reporter construct[15]. The rationale was to find compounds, which decreased the reporter activity and, thus, the frequency of EGFP expressing cells below a threshold of 2% (K/EGFP, for threshold definition see also refs. [5,15]). We did not prioritize compounds that led to increased K/EGFP, since these were previously demonstrated to

be possibly associated with unspecific cytotoxic effects[5]. We were able to identify compounds, which yielded changes in transcriptional KDM5B levels upon compound treatment. The imaging screen was performed using an Opera High Content Screening system with confocal microplate imaging for readout and image analysis was performed using Columbus 2.4.0 (both PerkinElmer, Waltham, MA, USA). The major measuring parameter of our assay was the K/EGFP level detected per cell and per well in relation to the total number of surviving cells after a 72 h treatment with compounds. Appropriate cell numbers used in the screen were 1250 cells/well as determined by preliminary titration experiments with Draq5 identifying dead cells. Oligomycin (0.1 µg/ml) was used as a control for positive hits, i.e., compounds that decrease the fraction of K/EGFP-expressing cells, trichostatin A (20 ng/ml) as negative control that absolutely increases K/EGFP without significant cell death, and cisplatin (20 µM) as negative control that relatively increases K/EGFP by killing bulk cells[5]. The counter screen filtered out unspecific effects, i.e., only positive hits that were seen in WM3734$^{KDM5Bprom-EGFP}$ but not in WM3734$^{CMVprom-EGFP}$ control cells were considered specific.

The workflow comprised screening of 7500 synthetic compounds from several well-known compound libraries, including the ENZO FDA-approved drug library (ENZO, 640 compounds), Analyticon Discovery library (AD, 2329 compounds), ChemBioNet library (CBN, 2816 compounds), ComGenex library (CGX, 2437 compounds), and the Sigma-Aldrich Library of Pharmacologically Active Compounds (LOPAC, 1280 compounds). The mechanism of action of some of these compounds are reported and known to modulate kinase, protease, ion channel, and epigenetic regulators. Three hundred and thirty-nine primary hits (AD: 46 compounds; CBN: 205 compounds; CGX: 2 compounds; ENZO: 18 compounds; LOPAC: 68 compounds) were identified, which decreased K/EGFP-expressing cells <2% without changing cell numbers more than 20% as compared to the DMSO control. In the next hit confirmation step, these 339 hits were confirmed in dose–response titration experiments in three independent runs with quadruplicates at each compound concentration (0.312, 0.625, 1.25, 2.5, 5.0, and 10 µM). The activities for 9 out of the 339 compounds met the criteria for progression, namely acceptable dose–response curve quality and potency. Out of the nine validated hits, we chose one compound, 2-phenoxyethyl-4-(2-fluorophenyl)-2,7,7-trimethyl-5-oxo-1,4,5,6,7,8-hexahydroquinoline-3-carboxylate (termed Cpd1), to analyze the biological impact on melanoma cells. As a negative control for the biological assays, we selected a structural analog compound (Neg4) that has a Molecular ACCess System (MACCS) similarity of 0.899, which was not identified as an hit compound (oxolan-2-yl)methyl-4-(6-bromo-2H-1,3-benzodioxol-5-yl)-2,7,7-trimethyl-5-oxo-1,4,5,6,7,8-hexahydroquinoline-3-carboxylate).

Chemical analysis of Cpd1. Chemical structure of Cpd1 (2-phenoxyethyl 4-(2-fluorophenyl)-2,7,7-trimethyl-5-oxo-1,4,5,6,7,8-hexahydroquinoline-3-carboxylate, PubChem name BAS00915510) was analyzed in NMR (Supplementary Fig. 10). ^{1}H-NMR, ^{13}C-NMR, and ^{19}F-NMR were recorded on a DRX600 (600 MHz) spectrometer in MeOD.

Fura-2-based Ca^{2+} imaging. Cells were pretreated for 3–4 days in cell culture medium containing 10 µM Neg4 or Cpd1, if not indicated differently. Cells (80,000–100,000) were seeded on 25 mm round (No. 1.5, #6310172, VWR) glass coverslips 48 h before the experiment and were loaded with 1 µM Fura-2 AM (#F1221, Thermo Fisher Scientific GmbH, Schwerte, Germany) in growth medium (containing the indicated compounds) for 30 min at room temperature. The measurements were performed at room temperature in Ringer's buffer (pH 7.4) containing 145 mM NaCl, 4 mM KCl, 10 mM Glucose, 10 mM HEPES (4-(2-hydroxyethyl)-1-piperazineethanesulfonic acid), 2 mM MgCl$_2$ and 0.5 mM CaCl$_2$, or 0 mM CaCl$_2$ with 1 mM EGTA.

Fura-2-based measurements of cytosolic Ca^{2+} were performed using a Zeiss Axiovert S100TV equipped with a pE-340$_{fura}$ (CoolLED, Andover, UK) LED light source with LED 340 nm (excitation filter: 340/20) and 380 nm (excitation filter: 380/20) together with a T400 LP dichroic mirror and 515/80 emission filter, a sCMOS pco.edge camera and a Fluar ×20/0.75 objective. Basal cytosolic calcium levels were measured in Ringer's buffer containing 0.5 mM Ca^{2+}, depletion of ER stores was achieved by perfusing calcium free Ringer's buffer with Thapsigargin (Tg, 1 µM) and Store-Operated Calcium Entry (SOCE) by re-addition of 0.5 mM Ca^{2+}. Data were analyzed with VisiView® Software (Visitron Systems GmbH, Puchheim, Germany). The obtained 340/380 nm fluorescence ratios were converted to calibrated data using the equation $[Ca^{2+}] = K^*(R - R_{min})/(R_{max} - R)$, while the values of K, R_{min}, and R_{max} were determined as described in Grynkiewicz et al.[56].

Determination of cell numbers and apoptosis. Cell numbers were assessed by MTT and crystal violet (CV) assays according to standard protocols[5]. Apoptosis was either detected by flow cytometry using LIVE/DEAD (Thermo Fisher Scientific, Waltham, MA, USA) or IncuCyte apoptosis assays (caspase 3, Annexin V, Essen Bioscience, Ann Arbor, MI, USA).

Clonogenic, limited dilution, and colony formation assays. 2D clonogenic growth was assessed after seeding 2500 (used for 5–7–9 days readout) or 300 cells (used for 9–16–20 days readout) per 24-well plate. Cells were treated and analyzed

by CV staining. Quantitation of melanoma self-renewal was done by limited (single-cell) dilution assays. In brief, cells were seeded at a density of one cell for every four wells in 96-well plates and grown for 19 days. Colony numbers were assessed microscopically by manual counting.

3D colony formation was assessed after 2500 cells had been embedded into 0.35% soft agar in six-well plates and grown over 30–52 days. Anchorage-dependent growth was inhibited by growing cells on a bed of 1% soft agar, with Tu2% or RPMI culture medium added on top and changed twice a week. For induction of KDM5B by doxycycline, WM3734$^{Tet3G-KDM5B}$ cells were pretreated with doxycycline for 24 h before seeding and then continuously treated for the duration of the assay. For induction of KDM5B by the chemical modulator, melanoma cells were either continuously treated with the designated concentrations of Cpd1 in soft agar until colonies reached 3 mm in size (day 25) or pretreated with 10 µM Cpd1 for 72 h before seeding in agar (pre-treatment). Colony numbers were assessed microscopically.

Collagen-embedded melanoma spheroids and cell invasion assays. Melanoma spheroids were generated as described previously[57]. In brief, 3000 cells were grown in each well of a 96-well plate on top a layer of non-adherent 1.5% agarose for 72 h to form spheroids. The spheroids were then individually collected and embedded in a collagen type I mixture to assess 3D invasion. Spheroids were imaged 10 days after collagen embedding using a Zeiss Axio Observer.Z1 microscope. Spheroid invasion was quantitated using ImageJ 1.48× software (NIH). Normalized invasion was quantified by subtracting the spheroid volume area from the invasion area. Representative pictures of melanoma spheroids are shown 10 days after collagen embedding. Neg4 vs. Cpd1 (10 µM) treatment was done either before collagen embedding of cells, or after completed spheroid formation, or before and after collagen embedding.

Immunostaining of tissues. Paraffin-embedded tumors or nevi were cut in 1.5, 2.5, or 4 µm sections. After deparaffinization and dehydration antibody staining was performed as indicated below or with silver nitrate working solution and fast red counterstain. Stained slides were scanned with an Aperio ScanScope AT2 (Leica) using ×20 objectives and selected regions were selected in Aperio Image-Scope software version 12.1.0.5029.

Immunostaining of KDM5B and MITF protein. Cellular stainings were either performed by chemical or fluorescent staining. For chemical immunostaining of KDM5B, cells were seeded onto glass coverslips, fixed in 4% PFA with 0.1% Triton X-100 for 10 min, and blocked with PBS containing 0.1% Triton X-100 plus 5% BSA for 30 min. Staining was performed using anti-KDM5B NB100-97821 (Novus Biologicals, St. Louis, MO, USA, 1:1200) and, as negative control, rabbit IgG (Dianova, Castelldefels, Spain, 1:1200). The Dako REAL Detection System (Agilent, Santa Clara, CA, USA) was subsequently applied according to the manufacturer's protocol and assessed using an Olympus BX51 or Zeiss AxioObserver.Z1 microscope. For immunostaining of KDM5B and MITF in FFPE tissue sections, slides were processed in a DAKO autostainer according to the manufacturer's protocol using the same antibodies or anti-MITF ab12039 (Abcam, Cambridge, UK, 1:1000). For immunofluorescence of KDM5B, cultured cells were fixed in 2% formalin containing 0.1% Triton X-100 for 15 min at room temperature (RT) followed by blocking with 5% BSA containing 0.1% Triton X-100 for 15 min at RT. Subsequent incubation with the primary antibody (1:1200 to 1:20,000) or rabbit IgG (1:1200 to 1:20,000, accordingly) was done for 1 h at RT. Alexa Fluor 568 goat anti-rabbit (1:600) served as secondary antibody. The staining was evaluated using a Zeiss AxioObserver.Z1 microscope and Zen software version 2.6. Image processing was applied equally across the entire image and was applied equally to controls.

Immunofluorescence staining of midbodies. WM164, WM3734$^{Tet3G-KDM5B-FKBP12}$, and WM3734$^{Tet3G-KDM5B}$ cells were grown in adherent subconfluent culture and treated with Cpd1 (10 µM), DMSO, Neg4 control (10 µM), or 10 ng/ml doxycycline for 72 h, respectively. Samples were fixed with 4% paraformaldehyde in BRB80 buffer (80 mM K-PIPES, pH 6.8, 1 mM MgCl$_2$, 1 mM EGTA) for 20 min, followed by three PBS washes and permeabilized with 0.25% Triton X-100 in PBS for 5 min. Samples were incubated in AbDIL (antibody dilution blocking buffer, 2% BSA, 0.1% Triton X-100, 0.1% NaN$_3$ in PBS) overnight at 4 °C. Primary antibodies to identify Aurora B kinase (1:100, AIM1, 611082, BD Biosciences, Franklin Lakes, NJ, USA), α-Tubulin (1:400, Abcam, Cambridge, UK), and phalloidin (1:100, Sigma-Aldrich, St. Louis, MO, USA) were diluted in AbDIL and incubated overnight. Samples were washed three times prior to the addition of secondary antibodies diluted (1:500) in AbDIL containing 4′,6-diamidine-2′-phenylindole dihydrochloride (1:1000, Sigma-Aldrich, St. Louis, MO, USA) for 1–2 h at RT. Samples were rinsed three times in PBS, 5 min each, and mounted in MOWIOL mounting medium (0.1 M Tris-HCl pH 8.5, 25% glycerol). Positive Aurora B Kinase and α-Tubulin-stained midbodies were either reported as a ratio of midbodies/cells per field of view, $n = 12$–16 fields or as midbodies/coverslip. One field of view consists of five images in width × 5 images in length. Images were acquired using a custom-built Nikon Spinning Disk Confocal[58] or a Zeiss Axio Observer.Z1 microscope at ×63 or ×100 magnification (numerical aperture of Nikon Spinning

Disk Confocal is 1.49, for AxioObserver.Z1 0.95 or 1.4). Coverslip (13 mm) images were acquired using an Axio Scan Z1 microscope at ×20 magnification. For the analysis each coverslip was subdivided into eight images. Normalization to cell counts were performed by DAPI counts in ImageJ 1.48x according to Shihan et al.[59]. Image processing was applied equally across the entire image and was applied equally to controls.

Quantitation of immunostaining. Immunofluorescence pictures were taken at ×20 magnification using a Zeiss Axio Observer.Z1 microscope (numerical aperture is 0.8). To determine mean intensities of KDM5B signals nuclear and cytoplasmic KDM5B signals from at least three representative pictures for each independent experiment were quantitated using CellProfiler version 3.1.8 (Broad Institute Broad Institute, Cambridge, MA, USA)[60]. Quantification of nuclear chromogen intensity of chemical immunostaining images was performed by using the reciprocal intensity method as published before[61]. Immunohistochemistry of tissue samples was scored following our previously published criteria by a certified histopathologist (K.G.)[62].

Flow cytometry. Flow cytometric analysis of KDM5B was done as described previously[16]. Briefly, cells were harvested and fixed in 2% formalin with 0.1% Triton X-100 in PBS for 20 min at RT followed by permeabilization in 90% methanol for 30 min at −20 °C. Primary (NB100-97821, Novus Biologicals, St. Louis, MO, USA or rabbit IgG, Dianova, Castelldefels, Spain) and secondary antibodies (Alexa Fluor 568 goat anti-rabbit IgG or Alexa Fluor 647 goat anti-rabbit IgG, Life Technologies, CA, USA) were incubated for 30 min at RT. Before and after antibody incubation, cells were washed with FACS buffer (PBS containing 0.5 M EDTA and 1% FBS). Samples were measured utilizing a Gallios flow cytometer (Beckman Coulter, Brea, CA, USA) and analyzed with Kaluza 1.2 (Beckman Coulter, Brea, CA, USA) or FlowJo V7.6.5 (Tree Star, Ashland, OR, USA) software. Gates were set based on the DMSO control, which was set to 1% KDM5B^high cells. For flow cytometric detection of KDM5B promoter-driven *EGFP* signals, WM3734^KDM5Bprom-EGPF cells were harvested, washed with FACS buffer, and stained for 7-AAD (eBioscience, San Diego, CA, USA). For quantitation, a 5%-threshold for the K/EGFP signal intensity was applied as described previously[5,15].

DNA content cell cycle profiling. Cell cycle analysis was performed by propidium iodide staining as described previously[15]. In brief, 100,000 MelJuSo, WM9, or SKMel5 cells were seeded per T75 flask or 20,000 WM3734 cells per 6 cm dish and starved for 5 days in medium without FBS. Starting from day 6, cells were treated for 72 h with Cpd1 either in the presence or in the absence of 2% FBS. WM3734^Tet3G-KDM5B clones (80,000 cells) were seeded per 6 cm dish and starved for 5 days. Starting from day 6, doxycycline (0, 1, 10, or 100 ng/ml) was added in FBS containing medium and replaced every 2–3 days. Cells were analyzed after 6 days of treatment. For propidium iodide staining, cells were trypsinised and washed with PBS containing 5 mM EDTA. Cells were then fixed with 100% ethanol for 30 min at RT followed by a RNase A treatment for 30 min at RT. Propidium iodide was added at a final concentration of 100 μg/ml. Quantitation was done on a Gallios cytometer (Beckman Coulter, Brea, CA, USA) in linear mode. Data analysis was performed using FlowJo V7.6.5 or Kaluza 1.2 software.

Single-cell cycle analysis. To generate stable melanoma cell lines expressing the FUCCI constructs, *mKO2-hCdt1* (30–120) and *mAG-hGem* (1–110)[63] were subcloned into a replication-defective, self-inactivating lentiviral expression vector system as previously described[49]. The lentivirus was produced by co-transfection of human embryonic kidney 293T cells. High-titer viral solutions for *mKO2-hCdt1* (30/120) and *mAG-hGem* (1/110) were prepared and used for co-transduction into melanoma cell line WM164 and subclones were generated by single-cell sorting[28,50].

Time-lapse microscopy. To track cell numbers, 80,000 WM3734 cells were seeded per 6-cm dish, and images were taken every 5 min over 5 days on 15 different areas per condition at ×10 magnification using a Zeiss Axio Observer.Z1 microscope. Cell numbers were manually counted for every position after 0, 24, 48, and 72 h of treatment. Cell division time was determined by measuring the time (in min) between cell rounding and complete abscission of daughter cells. FUCCI-WM164 cells[28] were grown in 24-well dishes and pretreated with Cpd1 (10 μM), Neg4, or DMSO for 24 h. Images for time lapse were acquired every 15 min over 96 h from five different positions in triplicate wells per experiment. Movies were captured at ×4 magnification using a live cell Olympus IX81 inverted microscope phase microscope equipped with a Hamamatsu ORCA-Flash2.8 camera. FUCCI probe fluorescence intensity over time was calculated as previously published[64] with the following modifications. Total duration and profile of FUCCI fluorescence of the different stages of the cell cycle were determined using the "spots function" in IMARIS version 8.4, Bitplane. A threshold for spots equal to or less than 15 μm were used to track fluorescent FUCCI nuclei utilizing the autoregressive motion algorithm. Track paths, following fluorescent nuclei, were then used to create regions of interest (ROI) and measure mean center point intensities throughout the duration of the movie. Tracks greater than 50% of the total movie duration were used for analysis to ensure full cell cycle profiles were captured. Tracks with breaks

greater than two frames were disregarded, and cells coinciding within 30 μm of peripheral X–Y borders were ignored to avoid including partial track profiles. Mean fluorescence intensity values were corrected for background fluorescence and used to calculate total track duration and generate plots of intensity variation over time.

Real-time quantitative RT-PCR (QPCR). Total RNA was isolated using the RNeasy Mini Kit according to the manufacturer's protocol (Qiagen, Venlo, Netherlands). Twenty nanograms RNA was used as a template for quantitative PCR with Precision OneStep qRT-PCR master mix (PrimerDesign, Southampton, UK) or Luna Universal One-Step RTqPCR Kit (NEB, Ipswich, MA). Quantitative PCR was performed with a StepOnePlus Real-Time PCR system (Thermo Fisher Scientific, Waltham, MA, USA). Thermal cycler conditions were 95 °C for 20 min, then 40 cycles of 3 min at 95 °C, followed by 30 s at 60 °C. The analysis was performed using the StepOnePlus software v2.1 (Thermo Fisher Scientific, Waltham, MA, USA). mRNA expression was calculated using the 2^−DDCT method and normalized to the housekeeping control 18S. Used primers are listed in Supplementary Table 3.

Immunoblotting. For immunoblotting of whole-cell lysates, cells were either lysed with RIPA buffer (50 mM Tris-HCl, pH 6.8, 150 mM NaCl, 0.5% sodium deoxycholate, 0.1% SDS, and 1% Triton X-100) supplemented with phosphatase inhibitors (cOmplete tablets; Roche Diagnostics) or according to the REAP protocol[65]. Samples (20–25 μg of protein) were separated on 8% polyacrylamide-SDS, wet transferred onto PVDF membranes (Roth, Karlsruhe, Germany) and blocked for 1 h in 5% milk containing 0.1% Tween-20. Primary antibodies (Axl (8661), CDH2 (13116), tubulin (2148), ZEB1/TCF8 (3396), Smad1 (9743), and TJP1 (8193; all diluted 1:1000, all Cell Signaling, Cambridge, UK), FKBP12 (ab24373), histone H3 (ab1791, diluted 1:5000), histone H3K4me3 (ab8580, diluted 1:2000), MITF (ab80651, diluted 1:500), and Notch1 (ab52627, all diluted 1:1000, all Abcam, Cambridge, UK), KDM5B (NB100-97821, diluted 1:2000, Novus Biologicals, St. Louis, MO, USA) and GAPDH (SC-510, diluted 1:5000, Santa Cruz, Dallas, TX, USA)) were incubated overnight at 4 °C either in PBS containing 0.1% Tween-20 and 5% milk or in 1× Net-G buffer (10× Net-G contains 1.5 M NaCl, 50 mM EDTA, 500 mM Tris 0.5% Tween-20, and 0.4% gelatine). Blots were washed with PBS-T or NetG followed by a 1 h incubation with horseradish peroxidase-conjugated secondary antibody (anti-rabbit (115-035-046) or anti-mouse (115-035-003, Jackson Immuno Research Laboratories, West Grove, PA, USA)) diluted 1:10,000 in PBS-T-milk 5% or NetG and a further washing step. Bands in western blots were visualized by an enhanced chemiluminescence system (WesternBright Chemiluminescence Substrate, Advansta, Menlo Park, CA, USA) and captured using a FUJI LAS3000 system. Digital quantitation was performed using ImageJ 1.48x software (NIH).

Ubiquitination assay. To detect protein ubiquitination the Signal-Seeker^TM Ubiquitination Detection Kit from Cytoskeleton (Denver, CO, USA) was used according to the manufactures' protocol. In short, cells were pretreated with either Cpd1 or Neg4 as control for 72 h before cell lysis. After immunoprecipitation of ubiquitinated proteins, lysates were analyzed by western blots using antiubiquitin (supplied by the kit), anti-GAPDH, or anti-KDM5B antibodies (see above).

In vivo studies. All animal experiments were performed in accordance with institutional and national guidelines and regulations. The protocols with a maximum tumor growth of 1500 mm³ have been approved by the local German authority Landesamt für Natur, Umwelt und Verbraucherschutz Nordrhein-Westfalen—LANUV NRW in compliance with the German animal protection law (Reference number AZ 84-02.04.2014.A08 AZ 81-02.04.2018.A202). The maximum tumor growth was not exceeded. The maximum tolerable dose of Cpd1 was determined in a prior experiment. Here, mice (n = 5) did not show abnormal behavior or body weight loss up to 100 mg/kg/day. Xenograft tumors of the human melanoma cell lines WM3734 or WM3734^Tet3G-KDM5B were generated by injection of 2 × 10⁵ cells in 200 μl medium (1:1 mixture of Tu2% with Matrigel® (BD Biosciences, Franklin Lakes, NJ, USA)) s.c. on the back of immunodeficient NMRI-(nu/nu)-nude mice (6–8 weeks old, both sex). WM3734^Tet3G-KDM5B xenograft model: once tumors reached 150 mm³ by caliper measurement (calculated as W×W×L/2), animals were randomized into two groups, "control" and "500 Dox," and the drinking water was supplemented accordingly with 2.5% sucrose plus 500 μg/ml doxycycline (provided ad libitum). Control mice received 2.5% sucrose-substituted water without doxycycline. Water was changed twice a week. WM3734 xenograft model: when tumors became palpable, animals were randomized into four groups, "control Cpd1" (100 mg/kg 3×/week (i.p.), "control TMECG" (10 mg/kg 5×/week (i.p.), "TMECG plus Cpd1 con" (10 mg/kg 5×/week and 100 mg/kg 3×/week, respectively), and "TMECG plus Cpd1 pre" (10 mg/kg 5×/week starting 7 days earlier and 100 mg/kg 3×/week, respectively). Tumor growth was measured three times a week using a caliper. Tumor samples were fixed in formalin for histological assessment and immunostaining. Xenograft tumors of the murine melanoma cell line CM[27] were generated by injecting 1 × 10⁵ cells in 200 μl medium (1:1 mixture of RPMI medium with Matrigel® (BD Biosciences, Franklin Lakes, NJ, USA)) s.c. on the back of female C57BL/6N mice (6–8 weeks old). Once tumors reached 400 mm³ by caliper measurement (calculated as W×W×L/2),

animals were randomized into two groups with each five mice, "Cpd1" (100 mg/kg) every second day intraperitoneal (i.p.), and "control group" (PEG300 + IgG, 250 µg every second day i.p.). Dosing continued until tumors had reached the maximal volume. Tumor samples were fixed in formalin for histological assessment and immunostaining.

RNAseq transcriptional profiling. For generating total RNA either WM3734 and CSM152 (100,000 cells) were seeded in a 6 cm dish and treated with Cpd1 (10 µM) or DMSO for 12, 24, 48, or 72 h. WM3734$^{Tet3G-KDM5B}$ (40,000 cells) were seeded in a 6 cm dish and induced with 10 ng/ml doxycycline for 24, 48, or 72 h. WM3734$^{Tet3G-shJARID1B}$ or as control WM3734$^{Tet3G-scramble}$ (175,000 cells) were seeded in a 6 cm dish and induced with 500 ng/ml doxycycline for 72 h. Total RNA was isolated using RNeasy Mini Kit according to the manufacturer's protocol (Qiagen Venlo, Netherlands). Barcoded stranded mRNA-seq libraries were prepared using the Illumina TruSeq RNA Sample Preparation v2 Kit (Illumina, San Diego, CA, USA) implemented on the liquid handling robot Beckman FXP2. Obtained libraries were pooled in equimolar amounts; 1.8 pM solution of this pool was loaded on the Illumina sequencer NextSeq 500 and sequenced uni-directionally, generating 500 million reads 85 bases long. The run was base called and demultiplexed using Illumina bcl2fastq2, version 2.20.0.422. The alignment was done using BWA mem, version 0.7.17. with default parameters. The reference genome for alignment was hg19 or in case of WM3734$^{Tet3G-shJARID1B}$ cells hg38. Finally, statistical gene set analysis was performed to determine differential expression at both gene and transcript levels. Partek Flow v6 defaults were used in all analyses. Gene set enrichment analysis (GSEA- http://software.broadinstitute.org/gsea/index.jsp) was performed using the pre-ranked tool version 4-6.012 (Broad Institute, Cambridge, MA, USA). All genes which contained an average of more than 1 read across all samples were used and ranked according to the T statistic. Gene sets were comprised of curated pathways from several databases including GO, Reactome, KEGG (24 March 2016 version; http://download.baderlab.org/EM_Genesets/current_release/Human/symbol/) and visualized using Cytoscape v3.7.2 (www.cytoscape.org; $p < 0.003$, $q < 0.04$, similarity cutoff 0.5). RNAseq of the cell lines WM3734 and CSM152 were analyzed separately and analyses were merged keeping only overlapping networks. Heatmaps were generated in Partek Genomic Suite or R using previously published genes sets[21,36–39,66]. Hierarchical clustering was performed by normalizing mean expression to 0 with a standard deviation of 1 and using Pearson's dissimilarity algorithm and average linkage. RNAseq data from skin cancers of TCGA[67] were downloaded from the Single Cell Portal (https://singlecell.broadinstitute.org). The violin plot was generated in BioVinci version 3.0.0.

Transcriptional profiling by microarray. RNA from melanoma cells (WM3734 stably infected with shKDM5B or as control scramble (SCR)[5] was extracted with Trizol reagent, followed by clean-up and DNase I treatment with Qiagen RNeasy mini kit in accordance with the prescribed protocol provided with the kit. Micorarray transcriptional analysis was performed using the HumanWG-6 v3.0 expression BeadChip sytem (Illumina, San Diego, CA, USA) at the Wistar Genomics facility. The data was processed with Illumina GenomeStudio Gene Expression Module version 2009.2 using defaults.

Sample preparation and clean-up for LC-MS. For LC/MS proteomic analysis, 400,000 WM3734 cells were seeded per 10 cm dish and treated on day 4 with Cpd1 (10 µM) or DMSO for 72 h. Cells were washed with PBS once before harvesting by mechanical detachment in PBS. Cells were centrifuged at $400 \times g$ for 4 min and the subsequent pellet resuspended in 120 µl lysis buffer (RIPA buffer (50 mM Tris-HCl, pH 6.8, 150 mM NaCl, 0.5% sodium deoxycholate, 0.1% SDS and 1% Triton X-100) supplemented with phosphatase inhibitors (cOmplete tablets, Roche Diagnostics)). After 30 min incubation on ice, lysates were centrifuged at $16,200 \times g$ for 30 min and the supernatant was stored at −80 °C. The samples were next reduced with DTT and alkylated with iodoacetamide and subsequently digested in the presence of sequencing grade LysC (Wako) and Trypsin (Promega, Fitchburg, WI, USA). Finally the acidified tryptic digests were desalted on home-made 2 disc C18 StageTips as described[68]. After elution from the StageTips, samples were dried using a vacuum concentrator (Eppendorf, Hamburg, Germany) and the peptides were taken up in 10 µl 0.1% formic acid solution.

LC-MS/MS settings. Experiments were performed on an Orbitrap Elite instrument (Thermo Fisher Scientific, Waltham, MA, USA)[69] that was coupled to an EASY-nLC 1000 liquid chromatography (LC) system (Thermo Fisher Scientific, Waltham, MA, USA). The LC was operated in the one-column mode. The analytical column was a fused silica capillary (75 µm × 30 cm) with an integrated PicoFrit emitter (New Objective) packed in-house with Reprosil-Pur 120 C18-AQ 1.9 µm resin (Dr. Maisch). The analytical column was encased by a column oven (Sonation) and attached to a nanospray flex ion source (Thermo Fisher Scientific, Waltham, MA, USA). The column oven temperature was adjusted to 45 °C during data acquisition. The LC was equipped with two mobile phases: solvent A (0.1% formic acid, FA, in water) and solvent B (0.1% FA in acetonitrile, ACN). All solvents were of UPLC grade (Sigma-Aldrich, St. Louis, MO, USA). Peptides were directly loaded onto the analytical column with a maximum flow rate that would

not exceed the set pressure limit of 980 bar (usually around 0.6–1.0 µl/min). Peptides were subsequently separated on the analytical column by running a 140 min gradient of solvent A and solvent B (start with 7% B; gradient 7–35% B for 120 min; gradient 35–100% B for 10 min; and 100% B for 10 min) at a flow rate of 300 nl/min. The mass spectrometer was operated using Xcalibur software (version 2.2 SP1.48). The mass spectrometer was set in the positive ion mode. Precursor ion scanning was performed in the Orbitrap analyzer (FTMS; Fourier transform mass spectrometry) in the scan range of m/z 300–1800 and at a resolution of 60,000 with the internal lock mass option turned on (lock mass was 445.120025 m/z, polysiloxane; see ref. [70]). Product ion spectra were recorded in a data dependent fashion in the ion trap (ITMS) in a variable scan range and at a rapid scan rate. The ionization potential (spray voltage) was set to 1.8 kV. Peptides were analyzed using a repeating cycle consisting of a full precursor ion scan (3.0×10^6 ions or 50 ms) followed by 15 product ion scans (1.0×10^4 ions or 50 ms) where peptides are isolated based on their intensity in the full survey scan (threshold of 500 counts) for tandem mass spectrum (MS2) generation that permits peptide sequencing and identification. Collision induced dissociation (CID) energy was set to 35% for the generation of MS2 spectra. During MS2 data acquisition dynamic ion exclusion was set to 120 s with a maximum list of excluded ions consisting of 500 members and a repeat count of one. Ion injection time prediction, preview mode for the FTMS, monoisotopic precursor selection, and charge state screening were enabled. Only charge states higher than 1 were considered for fragmentation.

Peptide and protein identification using MaxQuant. RAW spectra were submitted to an Andromeda[71] search in MaxQuant (1.5.3.30) using the default settings[72]. Label-free quantitation and match-between-runs were activated[73]. The MS/MS spectra data were searched against the Uniprot human reference database (UP000005640_9606.fasta, 70244 entries). All searches included a contaminants database search (as implemented in MaxQuant, 245 entries). The contaminants database contains known MS contaminants and was included to estimate the level of contamination. Andromeda searches allowed oxidation of methionine residues (16 Da) and acetylation of the protein N-terminus (42 Da) as dynamic modifications and the static modification of cysteine (57 Da, alkylation with iodoacetamide). Enzyme specificity was set to "Trypsin/P" with two missed cleavages allowed. The instrument type in Andromeda searches was set to Orbitrap and the precursor mass tolerance was set to ±20 ppm (first search) and ±4.5 ppm (main search). The MS/MS match tolerance was set to ±0.5 Da. The peptide spectrum match FDR and the protein FDR were set to 0.01 (based on target-decoy approach). Minimum peptide length was seven amino acids. For protein quantitation unique and razor peptides were allowed. Modified peptides were allowed for quantitation. The minimum score for modified peptides was 40. Label-free protein quantitation was switched on, and unique and razor peptides were considered for quantitation with a minimum ratio count of 2. Retention times were recalibrated based on the built-in nonlinear time-rescaling algorithm. MS/MS identifications were transferred between LC-MS/MS runs with the "match between runs" option in which the maximal match time window was set to 0.7 min and the alignment time window set to 20 min. The quantitation is based on the "value at maximum" of the extracted ion current. At least two quantitation events were required for a quantifiable protein. Further analysis and filtering of the results was done in Perseus v1.5.5.1[74]. For quantitation we combined related biological replicates to categorical groups and investigated only those proteins that were found in at least one categorical group in a minimum of five out of six biological replicates. Comparison of protein group quantities (relative quantitation) between different MS runs is based solely on the LFQs as calculated by MaxQuant (MaxLFQ algorithm; see ref. [73]).

Overall survival curves. Overall survival curves were calculated from the TCGA data set (http://cancergenome.nih.gov/) using UCSC Xena[75] or from a publicly available data set[76]. For the Kaplan–Meier plot patients were separated into low versus high expression of a KDM5 gene based on X-Tile version 3.6.1 cut-point optimization[77]. In case patients have donated multiple tissue samples, only one data set per patient was used. GraphPad Prism was used to create Kaplan–Meier survival curves and calculate hazard ratios (HR) with 95% confidence intervals and p values from log-rank tests.

Statistical analysis. Unpaired t-tests (Student's t-test) were used to compare mean differences between two independent groups. One-way ANOVA or two-way ANOVA was used to evaluate the association between a study outcome with multiple different treatment groups. The unpaired t-test, one-way and two-way ANOVA tests were performed in GraphPad Prism (versions 6-8), conducted at the two-sided significance level, where p values of ≤0.05 were considered significant. The tumor volumes of mice measured over time were used to reflect the tumor growth trend affected by different treatments. The velocities of tumor growth were compared between the treatments using a linear mixed-effect model with the random effect at individual animal level using R v.3.1 version. The differences between the tumor volumes of mice at the endpoint were evaluated by Mann–Whitney test. For GSEA the probability, which normalized enrichment scores represent a false-positive finding, was given as FWER (family-error rate) value.

Availability of materials. Except for Tet-On 3G-*KDM5B* and WM3734^Tet3G-shJARID1B cell lines, all materials are commercially available. The inducible Tet-On 3G-*KDM5B* and WM3734^Tet3G-shJARID1B cell lines are available upon request from the corresponding author (A.R.) via institutional MTA procedures.

Reporting summary. Further information on research design is available in the Nature Research Reporting Summary linked to this article.

Data availability

The mass spectrometry proteomics data generated in this study have been deposited in the ProteomeXchange Consortium via the PRIDE[78] partner repository (https://www.ebi.ac.uk/pride/archive/) under accession code PXD008757. The RNAseq data discussed in this study have been deposited in NCBI's Gene Expression Omnibus[79] database under accession codes GSE118529, GSE138068, and GSE168192. The microarray data generated in this study have been deposited in NCBI's Gene Expression Omnibus[79] database under accession code GSE137393. Data of The Cancer Genome Atlas TCGA data set [http://cancergenome.nih.gov/] were used for this study. In silico analysis of epigenetic data was performed with publicly available data sets and visualization using the IGV browser version 2.4.9 (refs. [80,81]). The following data sets were used: KDM5B-ChIPseq data from breast cancer cell lines SUM185, SUM159, MCF7, HCC2157, T47D, and MDA231 (GSE46073, ref. [42]), H3K4me3-ChIPseq data from melanoma cell lines MM27, MM13, MM16 (GSE71854, ref. [44]) and A375 (GSE99835, ref. [43]), and KDM5B- and H3K4me3-ChIPseq data from ChIP-Atlas[41]. The raw numbers for charts and graphs are available in the Source Data file whenever possible. Source data are provided with this paper.

References

1. Rambow, F. et al. Toward minimal residual disease-directed therapy in melanoma. *Cell* **174**, 843–855 e819 (2018).
2. Shaffer, S. M. et al. Rare cell variability and drug-induced reprogramming as a mode of cancer drug resistance. *Nature* **546**, 431–435 (2017).
3. Torre, E. A. et al. Genetic screening for single-cell variability modulators driving therapy resistance. *Nat. Genet.* **53**, 76–85 (2021).
4. Liau, B. B. et al. Adaptive chromatin remodeling drives glioblastoma stem cell plasticity and drug tolerance. *Cell Stem Cell* **20**, 233–246.e237 (2017).
5. Roesch, A. et al. Overcoming intrinsic multidrug resistance in melanoma by blocking the mitochondrial respiratory chain of slow-cycling JARID1B(high) cells. *Cancer Cell* **23**, 811–825 (2013).
6. Sharma, S. V. et al. A chromatin-mediated reversible drug-tolerant state in cancer cell subpopulation. *Cell* **141**, 69–80 (2010).
7. Wang, L. et al. An acquired vulnerability of drug-resistant melanoma with therapeutic potential. *Cell* **173**, 1413–1425 e1414 (2018).
8. Viswanathan, V. S. et al. Dependency of a therapy-resistant state of cancer cells on a lipid peroxidase pathway. *Nature* **547**, 453–457 (2017).
9. Rehman, S. K. et al. Colorectal cancer cells enter a diapause-like DTP state to survive chemotherapy. *Cell* **184**, 226–242 e221 (2021).
10. Hangauer, M. J. et al. Drug-tolerant persister cancer cells are vulnerable to GPX4 inhibition. *Nature* **551**, 247–250 (2017).
11. Shen, S. et al. Melanoma persister cells are tolerant to BRAF/MEK inhibitors via ACOX1-mediated fatty acid oxidation. *Cell Rep.* **33**, 108421 (2020).
12. Cierlitza, M. et al. Mitochondrial oxidative stress as a novel therapeutic target to overcome intrinsic drug resistance in melanoma cell subpopulations. *Exp. Dermatol.* **24**, 155–157 (2015).
13. Verduzco, D., Flaherty, K. T. & Smalley, K. S. Feeling energetic? New strategies to prevent metabolic reprogramming in melanoma. *Exp. Dermatol.* **24**, 657–658 (2015).
14. Roesch, A. et al. Retinoblastoma-binding protein 2-homolog 1: a retinoblastoma-binding protein downregulated in malignant melanomas. *Mod. Pathol.* **18**, 1249–1257 (2005).
15. Roesch, A. et al. A temporarily distinct subpopulation of slow-cycling melanoma cells is required for continuous tumor growth. *Cell* **141**, 583–594 (2010).
16. Yuan, P. et al. Phenformin enhances the therapeutic benefit of BRAF(V600E) inhibition in melanoma. *Proc. Natl Acad. Sci. USA* **110**, 18226–18231 (2013).
17. Wouters, J. et al. The human melanoma side population displays molecular and functional characteristics of enriched chemoresistance and tumorigenesis. *PLoS ONE* **8**, e76550 (2013).
18. Christensen, J. et al. RBP2 belongs to a family of demethylases, specific for tri- and dimethylated lysine 4 on histone 3. *Cell* **128**, 1063–1076 (2007).
19. Klose, R. J. et al. The retinoblastoma binding protein RBP2 is an H3K4 demethylase. *Cell* **128**, 889–900 (2007).
20. Yamane, K. et al. PLU-1 is an H3K4 demethylase involved in transcriptional repression and breast cancer cell proliferation. *Mol. Cell* **25**, 801–812 (2007).
21. Scibetta, A. G. et al. Functional analysis of the transcription repressor PLU-1/JARID1B. *Mol. Cell Biol.* **27**, 7220–7235 (2007).
22. Tan, K. et al. Human PLU-1 Has transcriptional repression properties and interacts with the developmental transcription factors BF-1 and PAX9. *J. Biol. Chem.* **278**, 20507–20513 (2003).
23. Bondeson, D. P. et al. Catalytic in vivo protein knockdown by small-molecule PROTACs. *Nat. Chem. Biol.* **11**, 611–617 (2015).
24. Nabet, B. et al. The dTAG system for immediate and target-specific protein degradation. *Nat. Chem. Biol.* **14**, 431–441 (2018).
25. Wang, J. et al. Calcium activates Nedd4 E3 ubiquitin ligases by releasing the C2 domain-mediated auto-inhibition. *J. Biol. Chem.* **285**, 12279–12288 (2010).
26. Park, J. Y., Jang, S. Y., Shin, Y. K., Suh, D. J. & Park, H. T. Calcium-dependent proteasome activation is required for axonal neurofilament degradation. *Neural Regen. Res.* **8**, 3401–3409 (2013).
27. Helfrich, I., Ullrich, N., Zigrino, P. & Schadendorf, D. Primary tumor versus metastasis: new experimental models for studies on cancer cell homing and metastasis in melanoma. *Pigment Cell Melanoma Res.* **27**, 309–316 (2014).
28. Haass, N. K. et al. Real-time cell cycle imaging during melanoma growth, invasion, and drug response. *Pigment Cell Melanoma Res.* **27**, 764–776 (2014).
29. Neto, H. & Gould, G. W. The regulation of abscission by multi-protein complexes. *J. Cell Sci.* **124**, 3199–3207 (2011).
30. Ben-Eliezer, I., Pomerantz, Y., Galiani, D., Nevo, N. & Dekel, N. Appropriate expression of Ube2C and Ube2S controls the progression of the first meiotic division. *FASEB J.* **29**, 4670–4681 (2015).
31. Mierzwa, B. & Gerlich, D. W. Cytokinetic abscission: molecular mechanisms and temporal control. *Dev. Cell* **31**, 525–538 (2014).
32. Asano, E. et al. SHCBP1 is required for midbody organization and cytokinesis completion. *Cell Cycle* **13**, 2744–2751 (2014).
33. Dey, B. K. et al. The histone demethylase KDM5b/JARID1b plays a role in cell fate decisions by blocking terminal differentiation. *Mol. Cell Biol.* **17**, 5312–5327 (2008).
34. Schmitz, S. U. et al. Jarid1b targets genes regulating development and is involved in neural differentiation. *EMBO J.* **30**, 4586–4600 (2011).
35. Zou, M. R. et al. Histone demethylase jumonji AT-rich interactive domain 1B (JARID1B) controls mammary gland development by regulating key developmental and lineage specification genes. *J. Biol. Chem.* **289**, 17620–17633 (2014).
36. Sarrio, D. et al. Epithelial-mesenchymal transition in breast cancer relates to the basal-like phenotype. *Cancer Res.* **68**, 989–997 (2008).
37. Gerber, T. et al. Mapping heterogeneity in patient-derived melanoma cultures by single-cell RNA-seq. *Oncotarget* **8**, 846–862 (2017).
38. Liberzon, A. et al. Molecular signatures database (MSigDB) 3.0. *Bioinformatics* **27**, 1739–1740 (2011).
39. Subramanian, A. et al. Gene set enrichment analysis: a knowledge-based approach for interpreting genome-wide expression profiles. *Proc. Natl Acad. Sci. USA* **102**, 15545–15550 (2005).
40. Tirosh, I. et al. Dissecting the multicellular ecosystem of metastatic melanoma by single-cell RNA-seq. *Science* **352**, 189–196 (2016).
41. Oki, S. et al. ChIP-Atlas: a data-mining suite powered by full integration of public ChIP-seq data. *EMBO Rep.* **19**, https://doi.org/10.15252/embr.201846255 (2018).
42. Yamamoto, S. et al. JARID1B is a luminal lineage-driving oncogene in breast cancer. *Cancer Cell* **25**, 762–777 (2014).
43. Joung, J. et al. Genome-scale activation screen identifies a lncRNA locus regulating a gene neighbourhood. *Nature* **548**, 343–346 (2017).
44. Bossi, D. et al. In vivo genetic screens of patient-derived tumors revealed unexpected frailty of the transformed phenotype. *Cancer Discov.* **6**, 650–663 (2016).
45. Saez-Ayala, M. et al. Directed phenotype switching as an effective antimelanoma strategy. *Cancer Cell* **24**, 105–119 (2013).
46. Ahmed, F. & Haass, N. K. Microenvironment-driven dynamic heterogeneity and phenotypic plasticity as a mechanism of melanoma therapy resistance. *Front. Oncol.* **8**, 173 (2018).
47. Su, Y. et al. Single-cell analysis resolves the cell state transition and signaling dynamics associated with melanoma drug-induced resistance. *Proc. Natl Acad. Sci. USA* **114**, 13679–13684 (2017).
48. Pospisil, V. et al. Epigenetic silencing of the oncogenic miR-17-92 cluster during PU.1-directed macrophage differentiation. *EMBO J.* **30**, 4450–4464 (2011).
49. Smalley, K. S. et al. Up-regulated expression of zonula occludens protein-1 in human melanoma associates with N-cadherin and contributes to invasion and adhesion. *Am. J. Pathol.* **166**, 1541–1554 (2005).
50. Spoerri, L., Beaumont, K. A., Anfosso, A. & Haass, N. K. Real-time cell cycle imaging in a 3D cell culture model of melanoma. *Methods Mol. Biol.* **1612**, 401–416 (2017).

51. Shannan, B. et al. Sequence-dependent cross-resistance of combined radiotherapy plus BRAF(V600E) inhibition in melanoma. *Eur. J. Cancer* **109**, 137–153 (2019).

52. Villanueva, J. et al. Concurrent MEK2 mutation and BRAF amplification confer resistance to BRAF and MEK inhibitors in melanoma. *Cell Rep.* **4**, 1090–1099 (2013).

53. Roesch, A. et al. RBP2-H1/JARID1B is a transcriptional regulator with a tumor suppressive potential in melanoma cells. *Int J. Cancer* **122**, 1047–1057 (2008).

54. Muhlenberg, T. et al. KIT-dependent and KIT-independent genomic heterogeneity of resistance in gastrointestinal stromal tumors—TORC1/2 inhibition as salvage strategy. *Mol. Cancer Ther.* **18**, 1985–1996 (2019).

55. Sanchez-del-Campo, L. et al. Synthesis and biological activity of a 3, 4, 5-trimethoxybenzoyl ester analogue of epicatechin-3-gallate. *J. Med. Chem.* **51**, 2018–2026 (2008).

56. Grynkiewicz, G., Poenie, M. & Tsien, R. Y. A new generation of Ca2+ indicators with greatly improved fluorescence properties. *J. Biol. Chem.* **260**, 3440–3450 (1985).

57. Smalley, K. S., Lioni, M., Noma, K., Haass, N. K. & Herlyn, M. In vitro three-dimensional tumor microenvironment models for anticancer drug discovery. *Expert Opin. Drug Discov.* **3**, 1–10 (2008).

58. Stehbens, S., Pemble, H., Murrow, L. & Wittmann, T. Imaging intracellular protein dynamics by spinning disk confocal microscopy. *Methods Enzymol.* **504**, 293–313 (2012).

59. Shihan, M. H., Novo, S. G., Le Marchand, S. J., Wang, Y. & Duncan, M. K. A simple method for quantitating confocal fluorescent images. *Biochem. Biophys. Rep.* **25**, 100916 (2021).

60. Carpenter, A. E. et al. CellProfiler: image analysis software for identifying and quantifying cell phenotypes. *Genome Biol.* **7**, R100 (2006).

61. Nguyen, D. H., Zhou, T., Shu, J. & Mao, J.-H. Quantifying chromogen intensity in immunohistochemistry via reciprocal intensity *Cancer InCytes* **2** https://protocols.scienceexchange.com/protocols/quantifying-chromogen-intensity-in-immunohistochemistry-via-reciprocal-intensity (2013).

62. Vogel, F. C. E. et al. Targeting the H3K4 demethylase KDM5B reprograms the metabolome and phenotype of melanoma cells. *J. Invest. Dermatol.* **139**, 2506–2516.e2510 (2019).

63. Sakaue-Sawano, A. et al. Visualizing spatiotemporal dynamics of multicellular cell-cycle progression. *Cell* **132**, 487–498 (2008).

64. Stehbens, S. J. et al. CLASPs link focal-adhesion-associated microtubule capture to localized exocytosis and adhesion site turnover. *Nat. Cell Biol.* **16**, 561–573 (2014).

65. Nabbi, A. & Riabowol, K. Rapid isolation of nuclei from cells in vitro. *Cold Spring Harb. Protoc.* **2015**, 769–772 (2015).

66. Tsoi, J. et al. Multi-stage differentiation defines melanoma subtypes with differential vulnerability to drug-induced iron-dependent oxidative stress. *Cancer Cell* **33**, 890–904.e895 (2018).

67. Corces, M. R. et al. The chromatin accessibility landscape of primary human cancers. *Science* **362**, https://doi.org/10.1126/science.aav1898 (2018).

68. Rappsilber, J., Mann, M. & Ishihama, Y. Protocol for micro-purification, enrichment, pre-fractionation and storage of peptides for proteomics using StageTips. *Nat. Protoc.* **2**, 1896–1906 (2007).

69. Michalski, A. et al. Ultra high resolution linear ion trap Orbitrap mass spectrometer (Orbitrap Elite) facilitates top down LC MS/MS and versatile peptide fragmentation modes. *Mol. Cell Proteomics* **11**, 013698 (2012). O111.

70. Olsen, J. V. et al. Parts per million mass accuracy on an Orbitrap mass spectrometer via lock mass injection into a C-trap. *Mol. Cell Proteomics* **4**, 2010–2021 (2005).

71. Cox, J. et al. Andromeda: a peptide search engine integrated into the MaxQuant environment. *J. Proteome Res.* **10**, 1794–1805 (2011).

72. Cox, J. & Mann, M. MaxQuant enables high peptide identification rates, individualized p.p.b.-range mass accuracies and proteome-wide protein quantification. *Nat. Biotechnol.* **26**, 1367–1372 (2008).

73. Cox, J. et al. Accurate proteome-wide label-free quantification by delayed normalization and maximal peptide ratio extraction, termed MaxLFQ. *Mol. Cell Proteomics* **13**, 2513–2526 (2014).

74. Tyanova, S. et al. The Perseus computational platform for comprehensive analysis of (prote)omics data. *Nat. Methods* **13**, 731–740 (2016).

75. Goldman, M. J. et al. Visualizing and interpreting cancer genomics data via the Xena platform. *Nat. Biotechnol.* **38**, 675–678 (2020).

76. Liu, D. et al. Integrative molecular and clinical modeling of clinical outcomes to PD1 blockade in patients with metastatic melanoma. *Nat. Med.* **25**, 1916–1927 (2019).

77. Camp, R. L., Dolled-Filhart, M. & Rimm, D. L. X-tile: a new bio-informatics tool for biomarker assessment and outcome-based cut-point optimization. *Clin. Cancer Res.* **10**, 7252–7259 (2004).

78. Vizcaino, J. A. et al. 2016 update of the PRIDE database and its related tools. *Nucleic Acids Res.* **44**, 11033 (2016).

79. Edgar, R., Domrachev, M. & Lash, A. E. Gene Expression Omnibus: NCBI gene expression and hybridization array data repository. *Nucleic Acids Res.* **30**, 207–210 (2002).

80. Townson, J. L. & Chambers, A. F. Dormancy of solitary metastatic cells. *Cell Cycle* **5**, 1744–1750 (2006).

81. Robinson, J. T. et al. Integrative genomics viewer. *Nat. Biotechnol.* **29**, 24–26 (2011).

Author contributions

H.C. and A.R. designed, planned, and evaluated the experiments and wrote the manuscript. H.C., B.S., S.M.D.-M., R.J.J., S.E., C.S.G., A.S., F.K., O.K., KJ, C.K., V.W.R., L.K., and I.H. performed the experiments. D.P., R.V., O.K., S.J.S., Q.L., X.Y., F.C.E.V., S.S.L., J.F., and S.H. performed analysis of genome-wide data, statistics, and the screening approach. M.R., M.E., A.P., J.C.B., I.H., D.R., M.K., M.H., I.B., J.N.R.-L., N.K.H., D.S., and A.R. supervised the project. B.S., C.S.G., S.M.D.-M., R.J.J., O.K., S.J.S., S.G., J.N.R.-L., and N.K.H. contributed to the design and interpretation of the experiments. All authors were involved in critical revision of the manuscript and approved the final submitted version.

Competing interests

The authors declare no competing interests.

Additional information

Supplementary information The online version contains supplementary material available at https://doi.org/10.1038/s41467-022-30641-9.

Correspondence and requests for materials should be addressed to Alexander Roesch.

Peer review information *Nature Communications* thanks Lin Deng, Shensi Shen and Qin Yan for their contribution to the peer review of this work.

Reprints and permission information is available at http://www.nature.com/reprints

Publisher's note Springer Nature remains neutral with regard to jurisdictional claims in published maps and institutional affiliations.

[1]Department of Dermatology, University Hospital Essen, West German Cancer Center, University Duisburg-Essen, Essen, Germany. [2]German Consortium for Translational Cancer Research (DKTK), Partner Site Essen/Düsseldorf, Essen/Düsseldorf, Germany. [3]The University of Queensland Diamantina Institute, The University of Queensland, Brisbane, QLD, Australia. [4]Division of Pediatric Neuro-Oncogenomics, German Cancer Research Center (DKFZ), Heidelberg, Germany. [5]Department of Pediatric Oncology, Hematology, and Clinical Immunology, Medical Faculty, University Hospital Düsseldorf, Düsseldorf, Germany. [6]Department of Neuropathology, Medical Faculty, Heinrich Heine University, Düsseldorf, Germany. [7]Molecular Physiology, Institute of Cardiovascular Physiology, University Medical Center, Georg-August-University, Göttingen, Germany. [8]Institute for Biomedical Engineering, Department of Cell Biology, RWTH Aachen University Medical School, Aachen, Germany. [9]Department of Chemical Biology, Faculty of Biology, University of Duisburg-Essen, Essen, Germany. [10]Center for Medical Biotechnology (ZMB), University of Duisburg-Essen, Essen, Germany. [11]Fraunhofer Institute for Translational Medicine and Pharmacology ITMP, Schnackenburgallee 114, 22525 Hamburg, Germany. [12]Fraunhofer Cluster of Excellence for Immune-Mediated Diseases CIMD, Schnackenburgallee 114, 22525 Hamburg, Germany. [13]The Wistar Institute, Philadelphia, PA, USA. [14]Faculty of Chemistry and Chemical Biology, TU Dortmund University, Otto-Hahn-Strasse 4a, 44227 Dortmund, Germany. [15]Translational Skin Cancer Research (TSCR), German Cancer Consortium (DKTK), University Hospital of Essen, Universitätsstrasse 1, 45141 Essen, Germany. [16]Institute for Developmental Cancer Therapeutics, West German Cancer Center, University Hospital Essen, 45122 Essen, Germany. [17]Department of Human Genetics, University Hospital Essen, University Duisburg-Essen, Hufelandstrasse 55, 45122 Essen, Germany. [18]Department of Microbiology, University of Duisburg-Essen, Universitätsstraße 2, 45117 Essen, Germany. [19]GENZ-Group of Research on Enzymology, Department of Biochemistry and Molecular Biology-A, Regional Campus of International Excellence 'Campus Mare Nostrum', University of Murcia, Murcia, Spain. [20]Present address: Division of Tumor Metabolism and Microenvironment, German Cancer Research Center (DKFZ), Im Neuenheimer Feld 280, 69120 Heidelberg, Germany. ✉email: alexander.roesch@uk-essen.de